Quantum Electronics **52** (5) 407–425 (2022)

NONLINEAR OPTICS

https://doi.org/10.1070/QEL18037

To the 60th Anniversary of Nonlinear Optics and the 60th Anniversary of the Scientific School of Nonlinear Optics at the Moscow State University

Optical second harmonic generation: role of symmetry and local resonances (review)

I.M. Baranova, T.V. Dolgova, I.A. Kolmychek, A.I. Maydykovskiy, E.D. Mishina, T.V. Murzina, A.A. Fedyanin

Abstract. **We report some results of studying optical second-harmonic generation (SHG) on surfaces and at interfaces of centrosymmetric media, in resonant nano- and microstructures, and in ferroelectric materials. The research was carried out at the Department of Quantum Electronics of the Lomonosov Moscow State University under the supervision of Professor O.A. Aktsipetrov, and subsequently developed by his disciples. As examples that clearly demonstrate the possibilities of the SHG method for examining nonstandard objects of nonlinear optics, we discuss the behaviour of the nonlinear optical response of single-crystal silicon and germanium surfaces and their interfaces with oxides, as well as nonlinear electroreflection. Optical interferometry and its possibilities are briefly described using the example of these systems. Unique sensitivity of SHG to the symmetry and resonance properties of nanostructures, including magnetic ones, is shown, which determines the efficiency of this method for investigating such systems. Finally, we demonstrate that the SHG effect is a unique remote and sensitive method for studying ferroelectric structures.**

Keywords: *second harmonic generation, symmetry, local field factor, resonant optical effects.*

1. Introduction

Optical harmonic generation, in particular second harmonic generation (SHG), is one of the classical and most studied effects in nonlinear optics. As is known, SHG was discovered in a crystalline quartz crystal by Franken et al. [1]. Soon, high sensitivity of the SHG method to the parameters of the surfaces of centrosymmetric media [2], and then to their hidden interfaces [3], was demonstrated. This property determines the unique possibilities of the SHG method for studying surfaces of different nature, which have been demonstrated for a number of structures. The first works in a similar field were performed simultaneously by foreign researchers and by R.V. Khokhlov and S.A. Akhmanov first at the Chair of Wave Processes, then at the Chair of Quantum Radiophysics (currently Quantum Electronics) of the Lomonosov Moscow State University; the laboratory was established in 1980 with the active support and participation of L.V. Keldysh, and headed by Oleg Andreevich Aktsipetrov (1947–2011). The main research topic of the laboratory was the study of the nonlinear optical phenomena discovered at nearly that time – giant Raman scattering of light and giant second harmonic (SH), which marked the beginning of a real boom in this field [4]. Indeed, the discovery of a giant (by 6–8 orders of magnitude) increase in the SHG intensity and Raman scattering of light in some metal and semiconductor nanostructures has led to the rapid development of both experimental and theoretical studies of the nonlinear optics of surfaces of centrosymmetric media. In fact, the work carried out in the 1980s laid the foundation for the direction of surface nonlinear optics, which is being actively developed today.

The idea of the surface SHG method is based on the sensitivity of this process to the symmetry of the medium and, in particular, to the breaking down of the inversion centre in the presence of an interface between centrosymmetric media. The higher rank of the susceptibility tensor describing this three-wave process determines the possibility of observing more complex symmetry properties of structures than in the case of a linear optical response [5]. Moreover, in the case of nonlinear optical interaction, the feasibilities of spectroscopic studies are also expanded – resonance effects both at the probe frequency and at the pump frequency manifest themselves in an increase in the nonlinear optical conversion efficiency [6, 7].

The aim of this review is to demonstrate the unique possibilities of the SHG method for studying various types of structures based on centrosymmetric materials, i.e. silicon and silver single crystals, structures with local resonances, and photonic and plasmonic crystals; the results of both fairly early work and those carried out over the past few years are presented.

I.M. Baranova Bryansk State Engineering Technological University, prosp. Stanke Dimitrova 3, 241037 Bryansk, Russia;
T.V. Dolgova, I.A. Kolmychek, A.I. Maydykovskiy, T.V. Murzina, A.A. Fedyanin Faculty of Physics, Lomonosov Moscow State University, Leninskiye Gory 1, stroenie 2, 119991 Moscow, Russia; e-mail: murzina@mail.ru;
E.D. Mishina MIREA – Russian Technological University, prosp. Vernadskogo 78, 125412 Moscow, Russia

Received 21 February 2022
Kvantovaya Elektronika **52** (5) 407–425 (2022)
Translated by I.A. Ulitkin

2. SHG sources in centrosymmetric media, symmetry of nonlinear susceptibility tensors

2.1. Phenomenological description of SHG

The main property of the SHG process, as well as of other nonlinear optical effects of an even order, is the forbiddance on the existence of the corresponding nonlinear optical response tensors in the electric dipole approximation in the bulk of centrosymmetric media [6]. However, symmetry

breaking in a near-surface layer with a thickness on the order of the lattice constant leads to the appearance of a surface dipole susceptibility, $\hat{\chi}^{(2)}_{\text{surf}} \neq 0$, which is the main source of SHG in the absence of a contribution from the bulk of matter. In this case, we are not talking about phase matching, since the second-harmonic quantum yield is small (about 10^{-13} in the case of a smooth silver surface); nevertheless, the second harmonic generation can be detected experimentally and carries a large amount of information.

2.2. Local field effects in SHG

As is known, nanoscale structuring can lead to the appearance of additional resonant properties that are plasmonic in the case of metals in the visible spectral range, as well as to the emergence of Mie resonances in dielectric and composite structures, resonances in photonic or plasmonic crystals, and whispering gallery modes for axially symmetric structures. In this case, the *local* optical field in the region of nonlinear sources may differ from the incident field, and the SHG intensity is determined by the expression

$$I_{2\omega} \sim (\chi^{(2)})^2 L^2(2\omega) L^4(\omega) I_0^2,$$

where $L(2\omega)$ and $L(\omega)$ are the local field factors at the SH and pump frequencies, respectively; and I_0 is the intensity of the incident radiation. The nonlinear nature of the SHG effect leads to a quadratic dependence of $I_{2\omega}$ on $L(2\omega)$ and to a fourth power dependence on $L(\omega)$, i.e., near resonance, the growth of the nonlinear optical response is much stronger than that of the linear one. Taking into account the predominant localisation of SH sources in the near-surface region, this opens up wide opportunities for studying the resonant properties of interfaces and nanostructures. It should be noted that the SH response in resonant structures is determined not only by the increase in the local field factor, the symmetry and susceptibility of the $\chi^{(2)}$ tensor, but also by such linear optical effects as absorption and reflection at the pump and SH frequencies, as well as by the phase of the quadratic nonlinear response. In the case of several SH sources, their total response is determined by the interference of electromagnetic fields at the SH frequency, with the relative phase of these fields playing a decisive role, especially in the spectral vicinity of resonances.

2.3. Magnetic field-induced effects in SHG

Nonlinear magnetooptics began to develop actively in the second half of the 1980s, after the appearance of theoretical works on the study of nonlinear optical effects induced by a static magnetic field in the response of magnetic media [8]. For the first time, the generation of magnetic field-induced SH in films of yttrium iron garnet was experimentally observed in [9] that was published almost simultaneously with the well-known paper by R. Shen [10]. It was shown that the magnitude of the nonlinear optical effects in the SH response significantly, by one or two orders of magnitude, exceeds the corresponding linear optical analogues, i.e. the Faraday and Kerr magneto-optical effects [11]. The reason for this is that, in addition to the gyration vector itself, which determines linear magneto-optical effects, there arise additional components of the nonlinear susceptibility $\hat{\chi}^{(2)}_{M}$ (absent in nonmagnetic media), which are, in the first approximation, a linear function of the magnetisation M [10] and have the same order of magnitude as the nonmagnetic (so-called crystallographic) susceptibility $\hat{\chi}^{(2)}_{\text{cr}}$. In this case, it should be emphasised that the magnetisation, being an axial vector, does not remove the centre of inversion of the medium. Thus, it becomes possible to study the magnetic properties of regions with broken inversion symmetry, including surfaces and hidden interfaces of many ferromagnetics, as well as nanostructures [12].

3. Second harmonic generation at the surface of monocrystalline silicon

Silicon, the main material of modern microelectronics, is a centrosymmetric m3m crystal, which makes it possible to use the reflected SHG signal for multipurpose investigation of the silicon surface and nanostructures based on it. Nonlinear optical diagnostics of Si and Si structures has a set of advantages: high sensitivity and possibility of studying optical, electrophysical, crystallographic and other characteristics of objects. It is implemented remotely and *in situ,* and is nondestructive and noninvasive. The results of numerous experimental and theoretical works devoted to SHG in silicon and silicon nanostructures are summarised in monograph [13].

Such parameters of the SH wave as intensity, polarisation, and phase contain information about many properties of the objects in question, with the sensitivity of the reflected SH to the properties of the surface of centrosymmetric crystals, their interfacial boundaries, and microstructures based on them being of particular importance. Information about the objects under study can be obtained based on the analysis of the dependences of the SH parameters on various factors. These include angular and polarisation dependences (reflected SH anisotropy method), dependences on an applied static electric field [nonlinear electroreflection (NER) method], dependences on surface current, mechanical stresses, etc.

3.1. Relationship between the anisotropy of the reflected SHG intensity and the crystal structure of the surface

In one of the first works in the field of reflected SHG, Bloembergen et al. [2] argued that the reflected SHG signal from the surfaces of cubic crystals, as in the case of an isotropic medium, depends neither on the choice of the reflecting crystal face nor on the orientation of this face. Only 15 years later, in 1983, it was experimentally found that the reflected SHG signal in the case of cubic crystals (Si, Ge, etc.) is anisotropic and is determined both by the choice of the reflecting face of the crystal and by its rotation angle ψ relative to the normal [14, 15]. For the first time, analytical expressions for the intensity of anisotropic reflected SHG $I_{2\omega}(\psi)$ were presented in [15, 16]. The issue of the possibility of separating the contributions of the silicon surface and its volume in the case of anisotropic reflected SHG was first considered by Aktsipetrov et al. [15]. Relying on the performed symmetry analysis of the azimuthal angular dependences of the reflected SHG from the silicon surface (a layer with a thickness of about 1 nm) and bulk (thickness is determined by the depth of the skin layer), it was shown that under certain conditions, for a smooth surface of the (001) and (111) faces, the analysis of the angular dependences $I_{2\omega}(\psi)$ makes it possible to do this analytically, which was a very impressive result for an optical method. For the first time, the contribution of the Si and Ge surfaces to the nonlinear optical response was experimentally separated and an estimate was obtained for

the absolute value of the quadratic susceptibility of the Si surface: $|\chi^s| \approx 10^{-15}$ SGSE units.

A general analysis of the symmetry of the quadratic susceptibility of crystalline media shows that there is a general rule – a so-called s-prohibition, according to which the intensity of the isotropic s-polarised SH component is equal to zero for a nonlinear non-centrosymmetric layer of arbitrary symmetry, including any face of the m3m symmetry crystal; in other words, $I_{2\omega}$ must vanish at the minima of the angular dependence of the s-polarised reflected SHG. Violation of this prohibition was found already in [15], which was explained by the presence of surface roughness.

Thus, as a result of the studies performed, a method was proposed for noncontact real-time control of nano- and microroughness of the surfaces of technologically important semiconductors. It was shown that in measuring small-scale (commensurate with the atomic size) roughness, the anisotropic reflected SHG method has the same sensitivity as the traditional X-ray scattering method. Calculations of the azimuthal angular dependences of $I_{2\omega}(\psi)$ for various combinations of pump and SH polarisations, taking into account the anisotropic contributions to the nonlinear polarisation, $\boldsymbol{P}_{2\omega}(\psi)$, from the surface layer and from the bulk, were performed in [17, 18] for the (111), (001), and (110) faces of the m3m class crystals, and corresponding anisotropic and isotropic (independent of the angle ψ) components of the reflected SH polarisation and intensity were separated.

The deviation of the orientation of the silicon surface from any crystallographic face affects the azimuthal symmetry of its reflected SHG response. This manifests itself in the difference in the amplitudes of the SHG intensity maxima in the rotational anisotropic dependence. Schuhmacher et al. [19] proposed to use the technique of single-beam SH interferometry to diagnose the surface bevel. This is due to the fact that the presence of the surface bevel is more pronounced in the phase reflected SH measurements than in the intensity ones, and also due to the absence of the influence of the sample alignment inaccuracy, which introduces an instrumental function with first-order symmetry into the azimuthal dependences of the SHG intensity. Thus, measurements of interferograms at several pairs of points with different azimuthal rotations can accurately determine the presence or absence of a bevel in the orientation of the surface of centrosymmetric semiconductors.

3.2. Generation of anisotropic reflected SH at the interphase $Si-SiO_2$ interface

A series of works was carried out on the generation of anisotropic SHG from an oxidised Si surface, a thin-layer $Si-SiO_2$ structure that is especially relevant for microelectronics. The works in this direction have demonstrated, first of all, the high efficiency of the method of reflected anisotropic SHG for studying the atomic structure and electrophysical properties of a given interphase boundary, as well as the presence of mechanical stresses in it. Kulyuk et al. [20] used two approaches: the study of the polarisation or azimuthal dependences of $I_{2\omega}(\psi)$. It was found that the removal of the oxide layer by etching noticeably reduces the intensity of the reflected SHG signal and changes the shape of the angular dependences of $I_{2\omega}(\psi)$. To explain an increase in the nonlinear optical response of the oxidised $Si-SiO_2$ structure compared to a clean surface, it was proposed to take into account additional components of the nonlinear polarisation (NP) at the SH frequency $\boldsymbol{P}(2\omega) \equiv \boldsymbol{P}$: the stress-induced dipole component $\boldsymbol{P}_{str}$, the dipole NP in a thin near-surface layer non-centrosymmetric oxide $\boldsymbol{P}_{cr}$, and electrically induced NP $\boldsymbol{P}_E \equiv \hat{\chi}_E^{(3)}(2\omega = \omega + \omega + 0)\boldsymbol{E}(\omega)\boldsymbol{E}(\omega)\boldsymbol{E}_{dc}(0)$. Experiments to measure the time dependences of $I_{2\omega}(t)$ *in situ* during etching confirmed the need to take into account these components.

The authors of Refs [21, 22] studied the role of the interference of pump and SH waves in the oxide layer, which is very significant in the formation of the SHG signal from the $Si-SiO_2$ structure. Van Hasselt et al. [22] investigated the azimuthal dependences $I_{2\omega}^{ss}(\psi)$ and $I_{2\omega}^{pp}(\psi)$ (superscripts indicate the SH and pump polarisation, respectively) for the $Si(111)-SiO_2$ structure with an oxide layer thickness of 2–310 nm and an angle of incidence $\theta = 4-75°$. It was found (Fig. 1) that the intensity of the s-polarised SH with s-polarised probe radiation at the maximum of the azimuthal dependence of I_{max}^{ss} on the thickness L_{ox} of the oxide layer has an oscillating form typical of interference, and at some values of L_{ox}, a one can observe significant increase in the reflected SHG signal com-

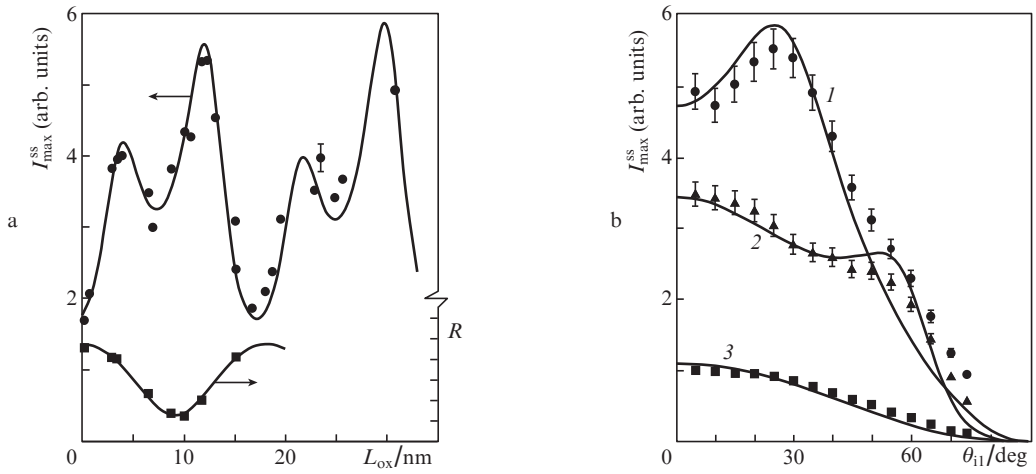

Figure 1. Experimental (points) and calculated (curves) dependences of I_{max}^{ss} (111) (pump incidence angle $\theta_i = 4°$) and linear reflection coefficient R on (a) the oxide thickness L_{ox} and (b) on the angle of incidence θ_{i1} at $L_{ox} = (1)$ 310, (2) 260, and (3) 2 nm.

pared to a sample with natural oxide. The dependence of I^{ss}_{max} on the angle of incidence at a sufficiently large SiO_2 thickness is nonmonotonic, which is also characteristic of interference. To explain the results, the authors of the work proposed a model of multiple reflection at the boundaries of the oxide film, which can be considered as a resonator capable of amplifying fields at frequencies ω and 2ω.

Works [23, 24] are the only ones that describe the manifestation of a fundamental physical phenomenon – the Casimir effect – in nonlinear optics. It was shown that under certain conditions, a large-scale nonlocality of the nonlinear optical response, the so-called Casimir nonlocality, can manifest itself, being the result of the interaction of a nonlinear medium with virtual photons of a quantised electromagnetic field. For a Si(111)–SiO_2–air(water) three-layer structure with an oxide layer as a resonator, the angular dependences (i.e., the intensity of the p-polarised SH upon p-polarisation of the pump) were measured, which were approximated by expression

$$I^{pp}_{2\omega}(L_{ox},\psi) = |\, a(L_{ox}) + c^{(3)}(L_{ox})\exp[i\Psi(L_{ox})]\cos 3\psi\,|^2.$$

Figure 2 shows the dependences of the isotropic component a, the amplitude of the anisotropic component of the reflected SH field $c^{(3)}$, and the phase shift Ψ between these components for the Si(111)–SiO_2 structures in air and in water on the oxide layer thickness L_{ox}. One can see, first, that for samples in air, one observes a pronounced dependence of the controlled parameters on the thickness of the oxide layer. Increasing L_{ox} to 50–100 nm leads to a sharp increase in all the parameters, which exhibit an oscillating dependence in the range of silicon oxide layer thicknesses L_{ox} = 100–300 nm.

Secondly, the suppression (smoothing) of these dependences is obvious when the samples are placed in an immersion medium, i.e. water. In this case, the Casimir interaction manifested itself in the size effect, i.e., the dependence of the reflected SHG signal on L_{ox}. It is important that the size effect associated with the Casimir interaction was distinguished against the background of size effects caused, for example, by the interference of pump or reflected SH waves.

3.3. Spectroscopy of the reflected SHG intensity of the silicon surface during hydrogen adsorption

The authors of Refs [25, 26] were the first to study nonlinear SH spectroscopy for a clean Si(001)2 × 1 surface (2 × 1 reconstruction) in the region of two-photon resonance E_1 (the doubled energy of the pump photon varied in the range $3 \leqslant 2\hbar\omega \leqslant 3.5$ eV) with changing temperature from 200 to 900 K, as well as during a deposition of 0 to 1.5 monolayers of hydrogen atoms. The experiments were performed in ultrahigh vacuum, using a pp-combination of pump and SH polarisations. For a hydrogen layer of constant thickness, an increase in temperature led to a red shift of the E_1 resonance and to its broadening. At a fixed temperature, an increase in the coating thickness from 0 to 1.0 monolayers led to a red shift, line shape distortion, and resonance suppression, while a further increase in the thickness from 1.0 to 1.5 monolayers led to a blue shift of the resonance. Dadap et al. [26] came to the conclusion that the correct interpretation of the experimental data and, in particular, the explanation of the suppression of the E_1 resonance during hydrogen adsorption require taking into account the removal of the surface mechanical stress, as well as the NER effect stemming from the appearance of a constant electric field in the near-surface Si region due to charge redistribution during hydrogen adsorption.

3.4. Interferometric spectroscopy of the amplitude and phase of the SHG reflected from the surface of group IV semiconductors

Interferometric SHG spectroscopy in frequency domain is a modern version of second harmonic amplitude and phase spectroscopy. In works [27–29], it was applied to study the

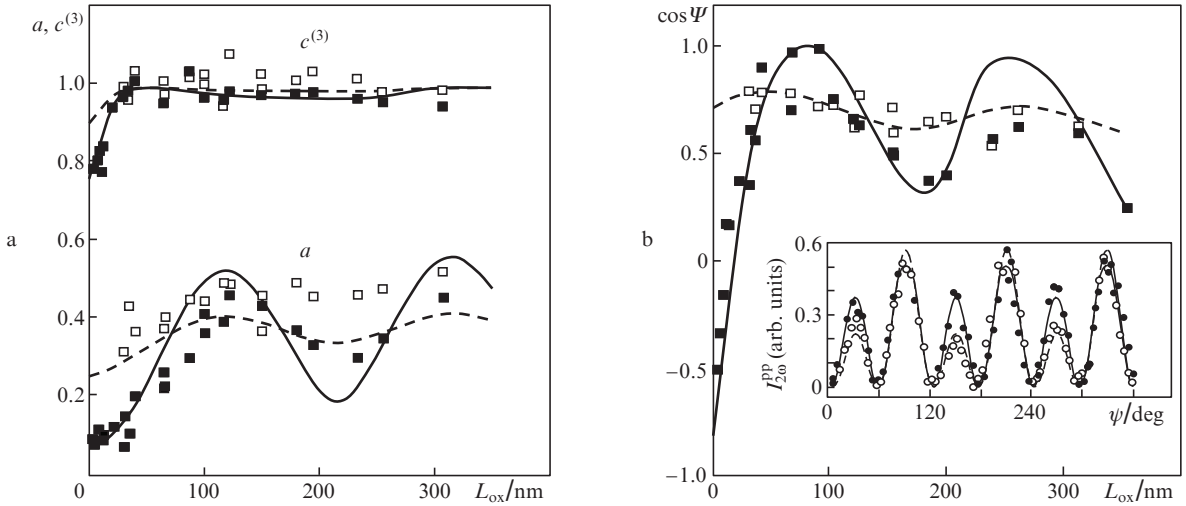

Figure 2. Experimental (squares) and calculated (curves) dependences of (a) the isotropic (a, bottom) and anisotropic ($c^{(3)}$, top) components of the reflected SH field and (b) of the cosine of the phase shift Ψ between these components on the oxide thickness L_{ox}; black squares and solid curves are samples in air; open squares and dashed curves are samples in water. The inset shows the angular dependences of the reflected SHG intensity $I^{pp}_{2\omega}$ (black circles and solid curve, L_{ox} = 34 nm; open circles and dashed curve, L_{ox} = 65 nm).

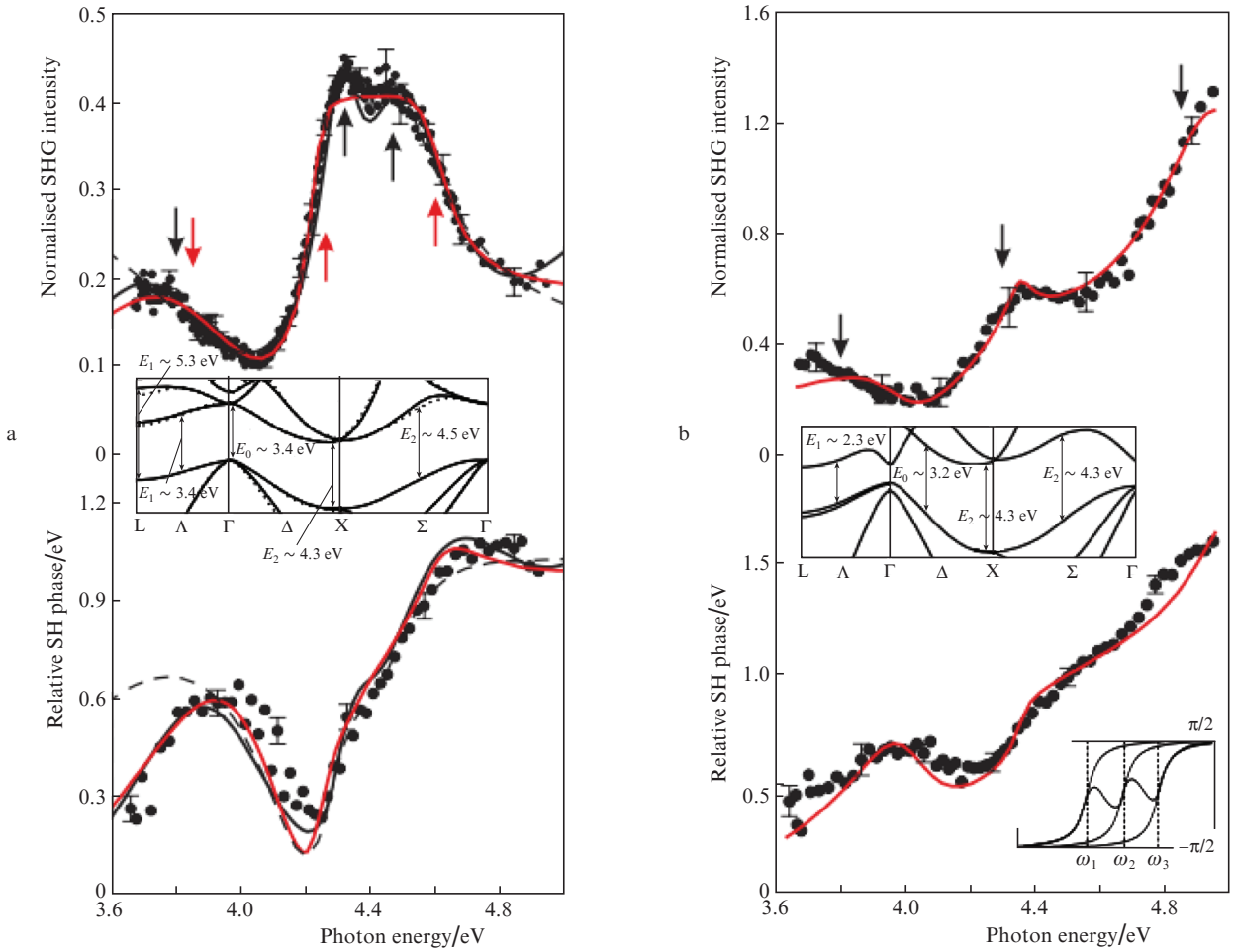

Figure 3. (Colour online) Experimental spectral dependences of the intensity and phase of the SH wave measured at intermediate points of the azimuthal dependence for (a) silicon and (b) germanium. Solid black curves are the joint approximation of the amplitude and phase spectra in the model that takes into account three exciton critical points; dashed curves are the result of the approximation of only the intensity spectrum and the phase spectrum calculated from the obtained values of the fitting parameters; solid red curves are the result of a joint approximation with two-dimensional line shapes for the main resonances. The insets show the band structures of the corresponding crystals and a diagram of the relationship between resonances.

resonant response of Si(111) and Ge(111) surfaces with natural oxide. The spectral dependences of the SH amplitude (intensity) and phase were measured in the SH photon energy range from 3.6 to 5 eV (Fig. 3).

Resonance features were found in the spectra resulting from direct electronic transitions on the surface in the vicinity of the critical point E_2 of the band structure of the bulk of silicon and germanium in the vicinity of the SH photon energy of 4.3 eV. The SHG intensity and phase spectra reflect the behaviour of optical susceptibilities and Green's corrections. In the vicinity of resonances, it was important to take into account all the factors that demonstrate critical behaviour both at the pump frequency and at the SH frequency: in particular, Green's corrections, which significantly affect the result of calculating the interference of the bulk and surface contributions, including introducing an additional phase shift.

In this regard, the following model representations were used to describe the obtained experimental dependences. The normalised amplitude of the SH field was represented as

$$\frac{E(2\omega)}{E^2(\omega)} = G_{\parallel}\chi_{\parallel}^{(2)} + G_{\perp}\chi_{\perp}^{(2)},$$

where $G_{\parallel}$ and $G_{\perp}$ are Green's corrections for the SH field components parallel and perpendicular to the sample surface; and $\chi_{\parallel}^{(2)}$ and $\chi_{\perp}^{(2)}$ are the corresponding second-order effective nonlinear susceptibilities containing surface and bulk contributions. It was believed that the spectral dependences of these susceptibilities are due to the superposition of several resonant contributions associated with different critical points of the combined density of states of the silicon surface. In addition, the presence of two-dimensional and one-dimensional critical points was assumed, at which the $|E|(p)$ dependence has extrema along two or along one axis in p-space, respectively, while this dependence is monotonic along other axes. Two close resonances were found in the SHG intensity spectrum, as well as an increase in $I_{\max}$ at the edges of the studied spectral range was also revealed; these resonance features in the intensity spectrum correspond to sections of the spectral growth of the SH wave phase. In accordance with this, it was shown that the observed spectra are due to the superposition of four two-photon resonances, which indicates a complex mechanism for the formation of a nonlinear response of the $Si-SiO_2$ structure. It turned out that the parameters of the SH resonances in silicon with frequencies of 3.8 and 5.2 eV, close to the edge of the spectral range, are uniquely and stably

determined only by a combined analysis of the spectra of both the intensity and the phase of the SH wave. The critical point E_2 of the band structure of germanium has a two-dimensional type with a stepped line shape and a resonance frequency of 4.3 eV.

3.5. NER in semiconductors

The dependence of the reflected SHG intensity on the strength of the electric field applied to the silicon and silver surfaces was observed for the first time in [30]. Aktsipetrov and Mishina [31] used this phenomenon to study the nonlinear response of silicon and germanium. Aktsipetrov et al. [32, 33] demonstrated the wide possibilities of NER for the study of silicon. A significant step in the development of the NER method was the use of metal–dielectric–semiconductor structures instead of the electrochemical method of applying a static electric field, which greatly simplified the experiment and interpretation of the results. Simultaneously with the development of experimental techniques, ideas about the nature of the NER phenomenon were also improved. A great contribution to the development of the scientific foundations of the NER method was made in the series of works by O.A. Aktsipetrov and co-authors [3, 21, 34, 35]. Aktsipetrov et al. [3] were the first to use a MOS structure for the application of an electrostatic field in a transmission scheme and, in this case, the anisotropy of the nonlinear response in NER was taken into account. In papers [13, 18, 36], a detailed theory was presented that takes into account most of the factors determining the nonlinear optical response of a surface in the presence of a static electric field.

New possibilities for NER diagnostics are opened up by spectroscopy of silicon structures, in which, due to the action of a quasi-static field, electrically induced nonlinear polarisation is induced (so-called electric field induced SH spectroscopy). Work [37] is one of the first studies in which the effect of electric field induced SH on the spectrum of the second harmonic reflected from silicon structures was studied. The MOS structure of Si(001) – SiO2 – Cr was studied, and the spectral studies were combined with the analysis of the anisotropy of the reflected SHG. Two resonances were found in the spectral dependences of the anisotropic SHG intensity: a resonance at $2\hbar\omega = 3.26$ eV, which was independent of the metal electrode potential U, and a resonance at $2\hbar\omega = 3.37$ eV, which was electrically induced.

A comprehensive study of the $Si(001)–SiO_2–Cr$ structure with the simultaneous use of the methods of anisotropic reflected SHG, NER, and modulation spectroscopy was performed in [21]. This work gave a significant impetus to the development of the theoretical model of NER. First, the possibility of degeneracy of charge carriers was taken into account, and when calculating the field distribution in the space charge region (SCR), use was made of more general Fermi–Dirac statistics rather than of the Boltzmann statistics. Second, it was taken into account that, at a high carrier concentration, the thickness of the near-surface SCR becomes so small that quantum effects should be accounted for. Third, the possibility of intense photogeneration of nonequilibrium carriers was taken into account. Therefore, in calculating the field distribution in the SCR, use was made of one of the methods for the theoretical description of thermodynamically nonequilibrium systems, i.e. Fermi level splitting into two quasi-Fermi levels for electrons and holes.

Dolgova et al. [38] studied the electrically induced phase shift of the SH wave reflected from the $Si(111))–SiO_2–Cr$ structure by varying the voltage between the chromium electrode and the silicon; the measurements were carried out for a fixed pump wavelength of 1064 nm (Nd:YAG laser). To explain the experimental results, a model was proposed in which one more contribution to the nonlinear polarisation was introduced, i.e. the surface electrically induced contribution, $\boldsymbol{P}_{SE} = \hat{\chi}_{SE}\boldsymbol{E}(\omega)\boldsymbol{E}(\omega)\boldsymbol{E}_{SC}(0)\delta(z)$, where $\boldsymbol{E}_{SC}(0)$ is the static field on the surface silicon; $\hat{\chi}_{SE}$ is the tensor of the corresponding nonlinear susceptibility; and $\delta(z)$ is the delta function. The existence of this contribution was first reported in [39]. Note that Aktsipetrov et al. [32] demonstrated the possibility of separating the surface and bulk contributions to the SHG signal for the $Si(001)–SiO_2$ structure using anisotropic electrically induced SHG spectroscopy, taking into account the fact that all contributions to the nonlinear polarisation at the SH frequency are isotropic, with the exception of the 'bulk' quadrupole contribution. The hypothesis of the surface electrically induced contribution was developed in the aforementioned work [26].

3.6. Current-induced SHG

A quasi-stationary electric current flowing in a centrosymmetric semiconductor leads to breaking of the inversion symmetry of the electronic subsystem, resulting in the appearance of current-induced nonlinear polarisation $\boldsymbol{P}^J(2\omega, J) = \hat{\chi}^J(J)\boldsymbol{E}(\omega)\boldsymbol{E}(\omega)$, where J is the direct current density; and $\hat{\chi}^J(J) = \hat{\chi}^{(2)J}(J)$ is the corresponding quadratic dipole susceptibility tensor. The effect of the current-induced SH for heavily doped p-Si(001) was first experimentally observed in [33]. The idea of the experiment was again based on the symmetry properties of the nonlinear response of the Si(001) surface in the presence of a current. Two measurement geometries were identified, for one of which the current-induced SHG is allowed, for the other it is prohibited. Comparison of the results of experiments performed using these two schemes and using an additional SH source (homodyne) made it possible to observe the current-induced SHG component and estimate the maximum value of the current-induced quadratic susceptibility: $\hat{\chi}^J(J) \sim 3 \times 10^{-15}$ m V^{-1}. The current-induced SHG can be used to determine the direction and density of currents in the near-surface regions of semiconductor devices.

3.7. Reflected SHG in the presence of inhomogeneous macroscopic stresses

The reflected SH generation method is sensitive to the presence of mechanical micro- and macrostresses in silicon. This is due to the removal of the prohibition on SHG in the dipole approximation in deformed regions of silicon that lack the inversion symmetry, as well as to the effect of stress on the band structure of silicon and, thus, on its spectral properties. Of great interest is work [40], which experimentally investigates SHG in silicon under controlled application of external mechanical tensions. The contribution to the SHG signal that occurs under the action of mechanical stresses was observed, and it was experimentally proved that this contribution is associated precisely with stress-induced changes in the band structure of silicon.

3.8. SHG spectroscopy of silicon–silicon dioxide quantum wells

Modification of the band structure of a semiconductor by quantum size effects can be used to observe new nonlinear optical effects. As an example of the study of quantum size effects by SHG spectroscopy, one can cite an experimental study of the electronic spectrum of a series of periodic silicon–silicon dioxide quantum wells with widths of several angstroms [41].

It is important that the quantum wells were made of amorphous silicon, which removes the limitation on the difference between the band gaps of the layers, determining the depth of the quantum wells. Crystalline semiconductor superlattices are made only of materials that can be grown epitaxially on top of each other: to reduce mechanical stresses, the lattice constants of neighbouring layers must be close. Otherwise, the defect density is so high that the quantum size effects are levelled out. This imposes a limitation on the difference in the band gaps of the layers, which determines the depth of the quantum well. The effective band gap in the bulk of both amorphous and hydrogenated amorphous silicon can vary from 0.95 to 1.65 eV, depending on the preparation technique. Therefore, the resonance of the combined density of states also falls into this interval, and the observed features of the SHG spectrum can be associated with resonances at the pump wave frequency.

Figure 4 shows the intensity spectra of the p-polarised component of the SH radiation for semiconductor silicon–silicon dioxide quantum wells, whose thickness of the amorphous silicon layer in is 0.25, 0.5, 0.75, and 1.0 nm. For comparison, the upper plot shows the spectrum of the Si(100) single-crystal silicon substrate. All SHG spectra exhibit resonance features in the vicinity of 2.7 and 4 eV, in contrast to the substrate spectrum.

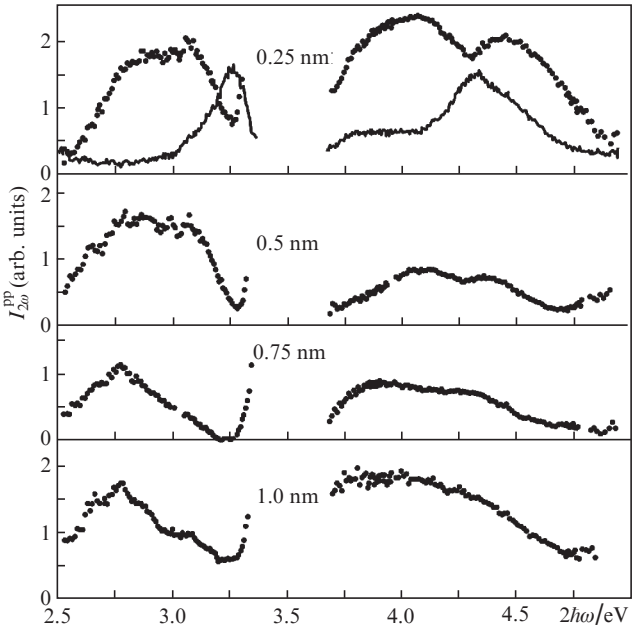

Figure 4. Intensity spectra of the isotropic component of p-polarised SH radiation. Dots are the spectra of SH reflected from semiconductor quantum wells with different thicknesses of the amorphous silicon layer (0.25–1.0 nm, shown in the figure). The solid curves in the upper panel are the spectra of the SH reflected from the (001) face of a single-crystal Si. (Based on the works of Avramenko V.G., Dolgova T.V., Nikulin A.A., Fedyanin A.A., Aktsipetrov O.A., Pudonin F.A., Sutyrin A.G., Prokhorov D.Yu., Lomov A.A. *Phys. Rev. B*, **73** (15), 155321 (2006); Fedyanin A.A. Doct. Diss. (Moscow: Lomonosov Moscow State University, 2009).)

The form of the SHG spectra of periodic quantum wells is determined by one- or two-photon direct electronic transitions between the energy subbands of a two-dimensional electron gas of amorphous silicon quantum wells. The shapes of the spectra reflect the shape of the line of the quadratic susceptibility of the two-dimensional electron gas. The thickness dependence of the resonance features is a consequence of the thickness dependence of the energy position of the subbands inside the well.

4. Resonance amplification of SHG in plasmonic nanostructures

Modern technologies make it possible to create artificial nanocomposite media with unique optical properties – from the resonance of local surface plasmons to induced negative refraction and the hyperbolic dispersion law. Let us consider the most striking effects found in the optical response of structures of different designs upon excitation of plasmon resonances of various nature.

4.1. Local surface plasmon resonance

Local surface plasmons (LSPs), i.e. light-induced collective oscillations of conduction electrons near the metal surface, can be excited in isolated or disordered metal nanoparticles of various shapes under the action of optical radiation. Interest in the study of LSPs sharply increased after the 1978 discovery of a giant amplification of Raman scattering of light by molecules located near a rough metal surface [4] or in colloidal solutions of metal nanoparticles, as well as the giant SHG in similar systems. It was soon shown that one of the main mechanisms of these effects is the amplification of the local electromagnetic field upon excitation of the LSP [42, 43], which demonstrated the important role of local resonances in increasing the efficiency of the nonlinear optical conversion for controlling the parameters of the quadratic nonlinear optical response.

4.1.1. SHG in silver island films. One of the first systems in which the role of plasmon effects in enhancing nonlinear optical effects, including the generation of optical harmonics, was studied were silver island films [44, 45] – disordered arrays of metal (Ag) nanoparticles fabricated by thermal deposition; depending on the mass thickness of the metal, d_m, the average size of nanoparticles, as well as the interparticle distance, changed. These parameters, as well as the distance between the metal nanoparticles and the substrate, determine the resonance frequency of the LSP; the island film is shown schematically in Fig. 5a. This substrate effect in the manifestation of LSP resonance in silver island films was demonstrated in [45]. The LSP resonance of silver nanoparticles on a Si/SiO_2 substrate, according to calculations, should be observed at a wavelength of about 270 nm, which corresponded to the region of tuning of the doubled radiation frequency of the optical parametric oscillator in the range of 490–680 nm.

The idea of the experiment was to smoothly change the distance between the silver island film and the silicon substrate by varying the thickness of the SiO_x layer while maintaining the other parameters of the silver island film structure

unchanged; a continuous Ag film with $d_m > 40$ nm was used as a reference structure in which the LSP resonance is not excited. The use of the SHG method excluded a significant contribution to the recorded signal from centrosymmetric materials, such as SiO_x and Si, and SHG in nonideal Ag nanoparticles was the dominant process.

The measured SHG intensity spectra for different oxide layer thicknesses (natural, $L_{SiO_x} = 70$ and 100 nm) are shown in Fig. 5a. One can see that an increase in L_{SiO_x} leads to (1) an increase in the amplitude of the SH spectral maximum and (2) its shift towards higher energies, which is 20 nm for a silver island film with $d_m = 1$ nm. According to the LSP resonance model in the silver island film presented in this work, the first of the noted features is associated with a decrease in the influence of the imaginary part of the silicon permittivity on the quality factor of the plasmon resonance, while the second one reflects a decrease in the effective permittivity of the medium surrounding the Ag nanoparticles with an increase in L_{SiO_x} [45]. Qualitatively similar dependences were obtained by third harmonic (TH) spectroscopy, which reflects the generality of the manifestation of LSP resonances in the nonlinear optical response of nanostructures.

4.1.2. Array of crescent-shaped nanoparticles. The anisotropy of the shape of plasmonic nanoparticles has a strong effect on the SHG parameters; this was shown, for example, in [46] using arrays of flat crescent-shaped gold nanostructures with a lateral size of about 200 nm (inset in Fig. 5b), fabricated by colloidal lithography. It is important that all nanoelements are oriented in the same way, despite their chaotic arrangement on the substrate, which ensures the anisotropy of the response of an ensemble of nanoparticles.

In the calculated and measured linear transmission spectra of such structures, three LSP resonances were found, the spectral position of which depends on the mutual orientation of the symmetry axis of the crescents and the polarisation plane of the probe radiation; they correspond to wavelengths of about 650, 890, and 2000 nm when the polarisation plane of the incident light is oriented along the crescent and in the orthogonal position at $\lambda_{1,2,3} = 690$, 1100, and 1400 nm [47]. Calculations have shown that the charge density distributions upon excitation of these resonances are fundamentally different, with the long-wavelength resonance corresponding to an electric dipole plasmon with the maximum localisation of the field near the sharp ends of the nanoelements.

Nonlinear optical experiments were performed at normal incidence of laser radiation, in the 'transmission' geometry. The azimuthal dependences of the SHG intensity were measured for parallel and crossed linear polarisations of the probe radiation and the SH.

It turned out that the shapes of the dependences $I_{2\omega}(\psi)$ change significantly when the wavelength of the probe radiation is tuned, which is especially noticeable in the case of crossed polarisations of the incident and detected radiation; the corresponding transmission spectrum is shown in Fig. 5b. Thus, in the short-wavelength region of the studied range, two SH maxima are observed per azimuthal rotation, and in the long-wavelength region, six, while the SHG intensity averaged over the azimuth angle increases with increasing wavelength, which is associated with the approach of the probe light wavelength to the LSP excitation spectral region .

According to the performed analysis, this is caused by a spectral change in the relative amplitude and phase of the effective components of the $\hat{\chi}^{(2)}$ tensor, which describe SHG in planar nanostructures, when the laser pump wavelength varies between the resonance LSP wavelengths λ_1 and λ_2, corresponding to different spatial configurations of the local electric field in nanoelements.

4.1.3. An array of nickel nanorods. Interesting effects were found in plasmonic nanostructures made of ferromagnetic metals [48]. The structures are arrays of nickel nanorods (with a diameter of 20 nm and a length of 175 nm) in an anodic alumina matrix oriented perpendicular to the substrate (inset in Fig. 5b). This structure combines magnetic and plasmonic properties, and LSP resonances can be excited across and along the rods; the corresponding wavelengths, according to calculations, are $\lambda_1 \approx 380$ nm and $\lambda_2 \approx 1150$ nm. At the same time, these resonance features did not manifest themselves in the linear reflection spectra, which is apparently due to significant ohmic losses in nickel and a low quality factor of the LSP resonances. Therefore, an attempt was made to visualise these features by the SHG method, using its symmetry capabilities, as well as its high sensitivity to the magnetic and resonance properties of nanostructures at the SH frequency.

The intensity spectra of the crystallographic (nonmagnetic) SH, $I_{2\omega}(\lambda)$, in the tuning region of a Ti:sapphire laser (730–880 nm), did not show a resonant increase in the SHG at $\lambda = 760$ nm, corresponding to the transverse LSP resonance at the double pump frequency, i.e., $2\lambda_1$, due to its low quality factor. Therefore, studied were the spectral features of the nonlinear optical response, namely, the magnetic contrast of the SHG intensity, defined as

$$\rho_{2\omega} = \frac{I_{2\omega}(\uparrow) - I_{2\omega}(\downarrow)}{I_{2\omega}(\uparrow) + I_{2\omega}(\downarrow)},$$

where $I_{2\omega}(\uparrow)$ and $I_{2\omega}(\downarrow)$ are the SH intensities measured in opposite directions of the static saturating magnetic field using the scheme of the transverse magneto-optical Kerr effect. It turned out that in the case of s-polarisation of the pump radiation, which provides the highest efficiency of excitation of the transverse LSP in nanorods, an increase in the magnetic contrast is observed in the vicinity of $\lambda = 760$ nm (Fig. 5c) due to the resonance amplification of the magnetically induced SH component, while in the case of p-polarisation of the pump radiation, the $\rho_{2\omega}$ spectra are monotonic. The symmetry analysis of the tensor $\hat{\chi}^{(2)}$ confirms this conclusion. Thus, the excitation of a transverse LSP in nanorods can only be detected when studying the magnetic field induced SH in a certain experimental geometry, which indicates a special sensitivity of nonlinear optical techniques to the resonant and magnetic properties of structures.

4.2. Structures with magnetic dipole plasmon resonance

Let us now consider SHG in structures with the so-called magnetic (dipole) resonance induced in nanoparticles of a more complex composition by the magnetic field of a light wave. The metasurfaces were a 2D square lattice with a period of 400 nm, at the nodes of which there were three-layer, Au/MgF_2/Au, nanodisks [49, 50]. The linear transmission spectra of this structure show two minima with centre wavelengths $\lambda_1 \approx 640$ nm and $\lambda_2 \approx 780$ nm (blue curve in Fig. 5d). Calculations in the CST Microwave Studio package demonstrated that at $\lambda = 640$ nm, the currents induced by pump radiation in two metal nanodisks are codirectional, and at $\lambda = 780$ nm, they are oppositely directed (see the diagram above Fig. 5d). This corresponds to the induction of an effective magnetic dipole in

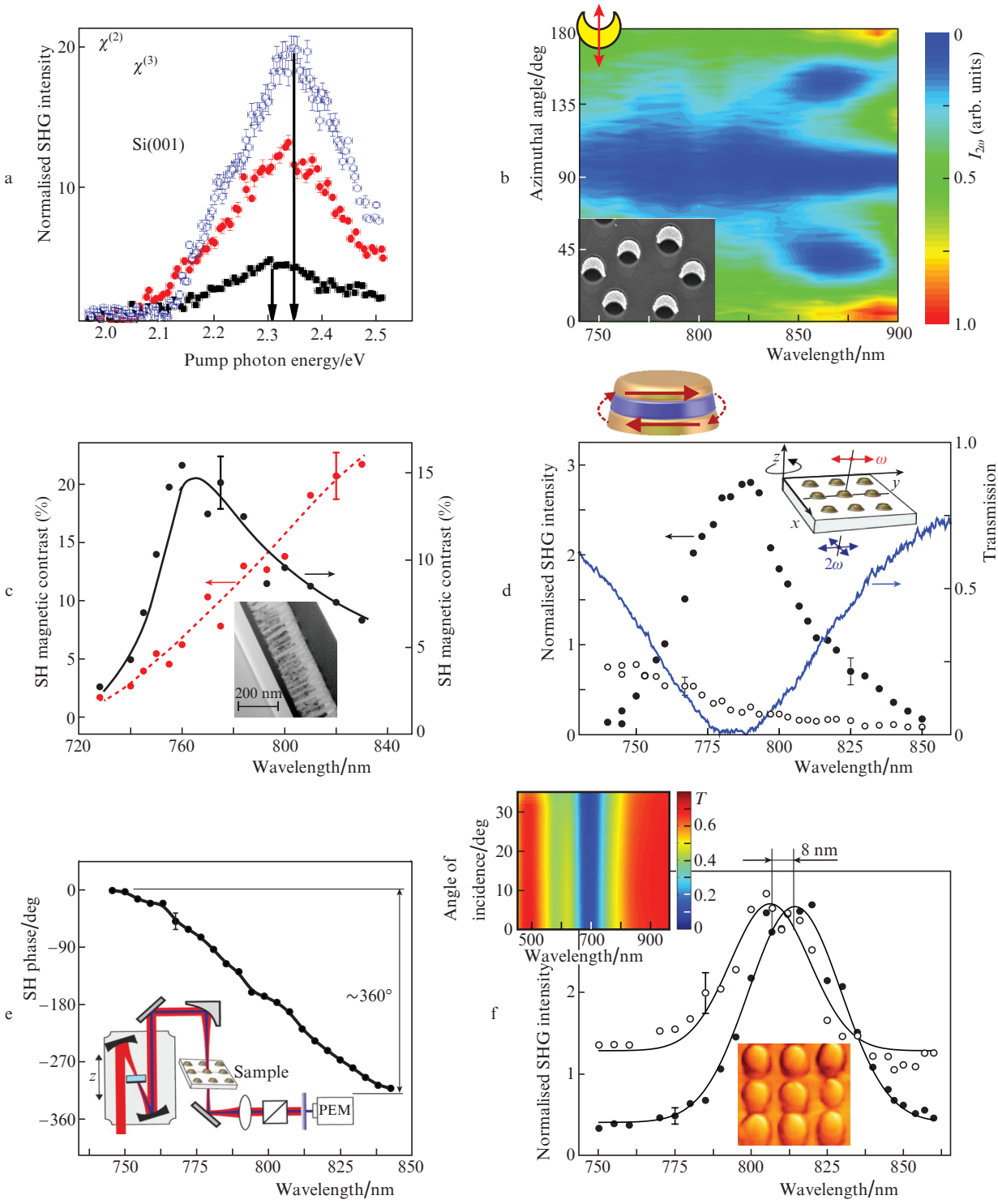

Figure 5. (Colour online) (a) Spectral dependences of the SHG intensity for silver island films deposited on a stepped oxide wedge at oxide layer thicknesses of (blue dots) 100 nm, (red dots) 70 nm, and (black dots) natural oxide (inset, structure diagram). (b) Azimuthal dependence of the SHG intensity in an array of golden crescents at crossed polarisations of the pump and SH radiation, $\psi = 0$ and 180°, corresponds to the situation when the polarisation plane of the laser radiation is oriented along the symmetry axis of the nanoelements (the inset shows the SEM image of the structure, the lateral particle size is about 200 nm [46]). (c) SH magnetic contrast spectra for p-polarised (left axis, red dots) and s-polarised (right axis, black dots) pump radiation in an array of nickel nanorods, incidence angle 45° (inset: the SEM image of sample cleavage [48]). (d) SHG intensity spectra in arrays of three-layer Au/MgF_2/Au nanodisks at normal incidence of pump radiation, parallel (black dots) and crossed (light dots) polarisations of laser radiation and SH; the blue curve is the transmission spectrum of the structure (the inset shows the scheme of the nonlinear optical experiment, at the top is the scheme of the element and the orientation of the currents in it upon excitation of the magnetic dipole resonance [50]). (e) SH phase spectrum in arrays of three-layer Au/MgF_2/Au nanodisks at normal incidence of pump radiation and parallel polarisations of laser radiation and SH (the inset shows the scheme of single-beam SH interferometry [50]). (f) SHG intensity spectra in an array of gold nanodisks coated with a Bi:YIG layer at opposite values of the transverse magnetic field, angle of incidence $\theta = 15°$, and p-polarised laser radiation (bottom inset, AFM image of the structure; upper inset, frequency-angular transmission spectrum of the sample under p-polarised probe radiation [51]).

the direction perpendicular to the current oscillation plane and a strong localisation of the electromagnetic field in the structure [52]. To increase the visibility of the resonant nonlinear response, the SHG spectroscopy was carried out in the 'transmission' geometry with normal incidence of the pump radiation on the structure (Fig. 5d); the cases of parallel (black dots) and orthogonal (light dots) polarisations of pump and SH radiation were considered. In the first case, a pronounced maximum was observed in the vicinity of the wavelength λ_2 corresponding to the spectral position of the magnetic dipole resonance. In the second case, the SHG intensity is approximately an order of magnitude lower, and the dependence $I_{2\omega}(\lambda)$ decreases monotonically, i.e., the resonance properties do not appear. These polarisation properties of the resonance dependence of the SH confirm the observation of the magnetic dipole resonance.

The spectrum of the SH phase upon excitation of a magnetic dipole resonance was measured by single-beam interferometry adapted to the case of tightly focused femtosecond radiation from a Ti:sapphire laser. The idea of the method is that the SHG signal from the structure under study interferes with the SH wave from the reference sample (etalon), which was an indium tin oxide (ITO) film placed at the focus of two spherical mirrors (see the diagram in Fig. 5e). The reference sample is placed on a translation stage, so that during the measurement the difference of optical paths at the pump and SH frequencies between ITO and the structure under study varies, while the measured value is the dependence of the SHG intensity on the reference coordinate z. The measured interferograms $I_{2\omega}(z)$ were approximated by a function of the form $I_{2\omega} \sim \cos(2\pi z/d + \varphi)$, from which the value of the SH phase φ was calculated; here d is the period determined by the air dispersion at the corresponding wavelength. It is not the absolute value of the SH phase that has a physical meaning, but its change during the transition of the laser radiation wavelength through the resonant features of the structures under study. It was found that upon excitation of a magnetic dipole resonance, the SH phase modulation is observed by almost 360° (Fig. 5e). Apparently, the main contribution to the SH generation at normal incidence of laser radiation is made by the magnetic dipole component $\chi^{\mathrm{emm}}_{yxx}$ (the coordinate axes are shown in the inset in Fig. 5d). When the pump wavelength passes through resonance, the phase of the corresponding local field factor changes by 180°, and so the field phase at the doubled frequency $E^{\mathrm{emm}}_{2\omega} \sim \chi^{\mathrm{emm}}_{yxx} L^2_x(\omega) B^2_x$ changes by 360° (B_x is the magnetic field component of the incident wave). This corresponds to the interferometry data and also confirms the resonant nature of the observed phenomena.

4.3. Lattice (diffraction) plasmon resonance

Another type of resonance response of an array of nanoparticles, the so-called lattice plasmon resonance (LPR), is observed in 2D arrays of metal nanoparticles with a period on the order of several hundreds of nanometres. Dipoles induced in periodically arranged metal nanoparticles by a linearly polarised light wave field radiate in phase in a certain direction, which leads to a multiple amplification of the scattered radiation compared to the response of an isolated particle. The dependence of this condition on the lattice parameters gave the name to this resonance feature. A corresponding increase in the SHG intensity was observed in 2D arrays of metal nanoparticles of various types [53], while we first discovered the LPR effect during the generation of the magnetically induced SH [54].

A 2D array of gold nanodisks located at the sites of a square lattice with a period of 400 nm, with a 100-nm-thick Bi:YIG magnetic dielectric layer, was studied. The combination of a ferromagnet and a plasmonic metal is a fairly popular technique for producing high-quality magnetoplasmonic structures that are interesting from the point of view of magnetic methods for controlling the optical response parameters by applying a static magnetic field to the structure [53]. An AFM image of the investigated LPR structure after its annealing, which is necessary for garnet crystallisation, is shown in the inset to Fig. 5f. The presence of an LPR in this structure manifests itself in the form of a transmission minimum at λ = 780 nm, which is independent of the angle of incidence in the case of p-polarised pump radiation (top inset in Fig. 5f).

The SHG intensity spectra obtained with p-polarised pump radiation and opposite values of the magnetic field are shown in Fig. 5f for an angle of incidence $\theta = 15°$. One can see that in the vicinity of the LPR, an increase in the SHG intensity is observed, and the SH maxima shift by approximately 8 nm when the sign of the applied magnetic field changes. The reason for this spectral behaviour of the magnetically induced SH is the presence of several interfering contributions to the SH, i.e. crystallographic and magnetic: resonant (from the Au/Bi:YIG interface) and nonresonant (from the air/Bi:YIG and quartz/Bi:YIG interfaces). The relative value and the phase shift between the corresponding fields at the SH frequency change significantly upon tuning the pump radiation wavelength in the spectral vicinity of the LPR, which causes a spectral shift of the resulting curve $I_{2\omega}(\lambda)$.

5. SHG in photonic crystals and microcavities

The term 'photonic crystal' (PC) was introduced for media with spatial periodic modulation of the permittivity in one, two or three directions. The simplest implementation of the PC is a 1D layered subwavelength periodic structure formed by alternating layers with refractive indices n_1 and n_2. There is a spectral region in which waves cannot propagate in a PC. It is called the photonic band gap (PBG), by analogy with the electronic band gaps in crystals, and is characterised by a maximum reflection coefficient and a minimum transmission, and its spectral position is determined by the optical thicknesses of alternating layers and shifts with a change in the angle of incidence of light on the structure. In a PC, in which a PBG centred at a wavelength of λ_0 is observed under normal incidence of light, the optical thickness of the layers is $\lambda_0/4$ [54]. If there is a defect in a periodic layered medium (usually a layer with an optical thickness of $\lambda_0/2$ is made), then this structure is called a microresonator (MR) (see the diagram in Fig. 6b), and a narrow spectral region appears in the PBG, called the microresonator mode, where there is a reflection minimum and a strong localisation of the electromagnetic field in the MR layer.

Interest in the nonlinear optical properties of PCs and MRs is due to two factors: at the PBG edges, due to strong dispersion, the phase-matching condition $\boldsymbol{k}_{2\omega} = 2\boldsymbol{k}_{\omega}$ can be satisfied, which will significantly increase the SHG efficiency; strong spatial localisation of the light field energy in the MR layer can lead to a significant increase in the SHG intensity.

Various options for the manufacture of PCs and MRs have been developed; however, the simplest implementation, which does not require expensive deposition techniques, are

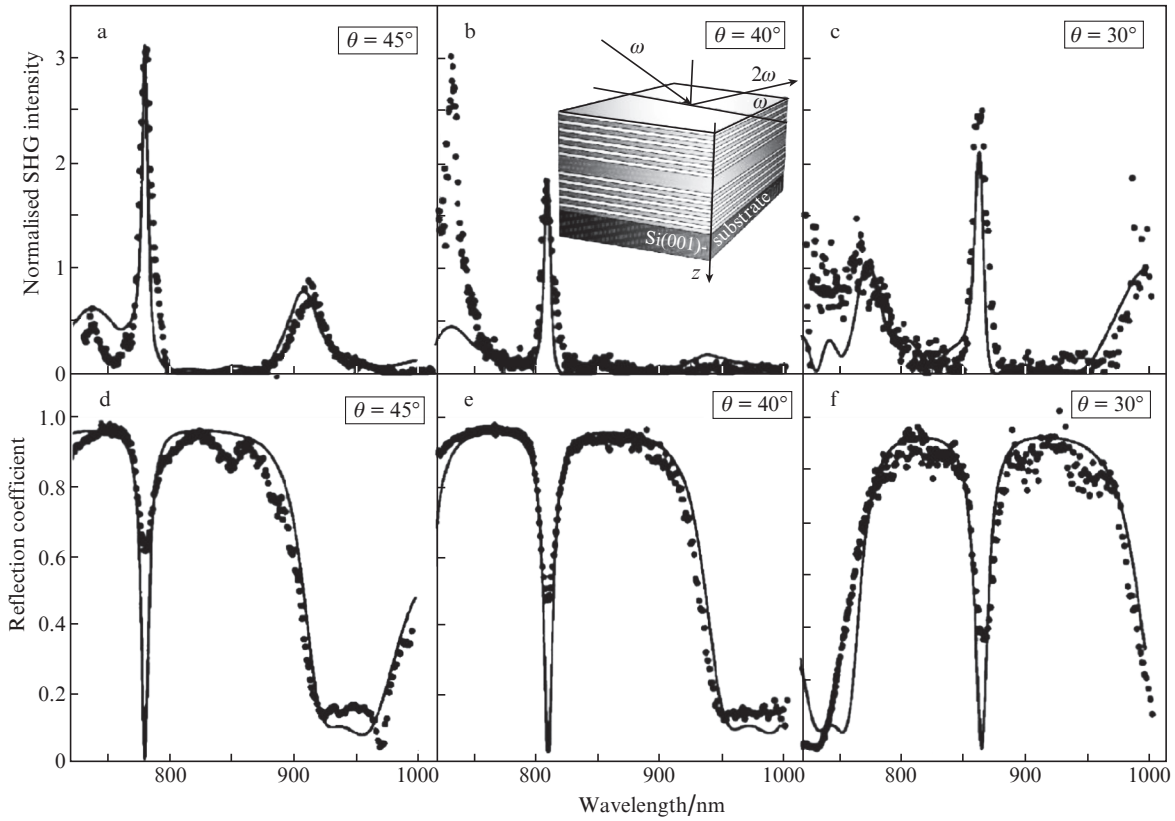

Figure 6. (a, b, c) Intensity spectra of reflected p-polarised SH in a microresonator based on porous silicon under s-polarised laser radiation and (d, e, f) reflection spectra of s-polarised light at different angles. The inset shows a diagram of a microresonator [55]. The values of the SHG intensity in panel (b) are increased by 7 times, and in panel (c), by 20 times. Solid curves are the results of model calculations.

structures based on porous silicon obtained by electrochemical etching of silicon (100) in a hydrofluoric acid solution. Varying the current density during etching makes it possible to control the porosity of the layers and, consequently, their refractive index.

The quadratic response of porous silicon PCs and MRs was studied in [55–60]. Figure 6 shows the SHG intensity spectra and the corresponding reflection spectra of the MR based on porous silicon at different angles of incidence of s-polarised probe radiation. These dependences demonstrate a significant enhancement of the SHG signal at the edges of the PBG (as a result of the closing of phase matching) and in the MR mode (due to field localisation in the MR layer). For example, at $\theta = 45°$, the enhancement of the SHG intensity in the MR mode reaches 500 times as compared with the values outside the PBG; at the long-wavelength edge of the PBG, the enhancement of $I_{2\omega}$ is much smaller and does not exceed 100. A decrease in the angle of incidence leads to a shift of all resonances to the long-wavelength region, which corresponds to the angular dependence of the spectral position of the PBG and the MR mode. In these works, it was also shown within the framework of the formalism of nonlinear propagation matrices that the resonances found in the MR mode are primarily due to the localisation of the pump field near the half-wave resonator layer (the field amplitude increases by a factor of four compared to the incident wave), and the resonant behaviour of the SHG intensity when the pump wavelength passes through the edge of the photonic band gap is due to a combination of two mechanisms: the fulfilment of the phase matching conditions at the edge of the photonic band gap and the enhancement of the pump field in the final photonic crystal (the amplitude doubles). Calculations show that the SH enhancement increases with an increase in the difference in porosity (permittivity) of the layers and an increase in the number of periods in photonic crystals, i.e. microresonator mirrors.

It should be noted that similar mechanisms lead to an increase in the TH at the edges of the PBG and in the MR mode in PCs and MRs [60, 61]. Subsequently, enhancement of nonlinear optical effects was also found in three-dimensional PCs based on artificial opals [62, 63].

6. Nonlinear optics of ferroelectrics

Ferroelectrics are materials that have spontaneous polarisation, the orientation of which can be changed by means of an external electric field. This ability to switch between two stable polarisation states is the basis for the development of nonvolatile ferroelectric random access memory (FeRAM) elements and electro-optical modulators. Ferroelectricity is inherent only in crystals in which the centre of inversion is broken; therefore, ferroelectrics occupy a special place in nonlinear optics. In particular, (commercial) harmonic generators are produced using ferroelectric crystals, such as barium beta-borate, lithium niobate, etc. On the other hand, the generation of the optical second harmonic is one of the most effective methods for studying these materials. While for harmonic generators it is fundamental to implement the phase matching condition, for diagnostic tasks this condition is, on the contrary, undesirable, since it can distort information about the material under study.

The fundamental (phenomenological) law, which is the basis for the diagnostics of ferroelectrics by the SHG method, is presented in [64]:

$$I_{2\omega} \propto \left| \hat{\chi}^{(2)}(\boldsymbol{P}) \vdots \boldsymbol{E}_\omega \boldsymbol{E}_\omega \right|^2 = \left| \hat{\chi}^{(3)}_P \vdots \boldsymbol{P} \boldsymbol{E}_\omega \boldsymbol{E}_\omega \right|^2, \quad (1)$$

where $\boldsymbol{P}$ is the dielectric polarisation. Publications on the experimental observation of SHG in ferroelectrics appeared almost immediately after the first observation of this effect [65, 66].

Ferroelectricity exists only in a certain temperature range. When the critical temperature (Curie temperature T_C) is reached, a structural phase transition occurs to a phase with a higher symmetry and, ultimately, to a paraelectric (centrosymmetric) phase. Since SHG is impossible in a centrosymmetric medium in the dipole approximation, this method is effective in studying phase transitions in ferroelectrics.

Ferroelectrics have a domain structure: they consist of uniformly polarised regions, whose (static) polarisation vector, in the general case, has an arbitrary direction. Since relation (1) is tensorial, the SHG efficiency from domains will be different.

6.1. Domain structure and ceramics: SH scattering

If the sizes of domains or micro-(nano-)crystallites of a ferroelectric are smaller than the wavelength, the SH scattering is an effective investigation method [64, 67]. A nonlinear optical technique based on joint measurements of the azimuthal dependences of the SHG intensity and scattering indicatrix was used to study textured $(PbZr)TiO_3$ (PZT) thin films in [68–71] and was further developed in [72]. Figure 7 shows the scheme of the experiment and the results obtained. The dependence $I_{2\omega}(\psi)$ is a superposition of a significant isotropic background and an anisotropic dependence with two maxima. All scattering indicatrixes were measured at the maximum and minimum of the anisotropic dependence. It was shown that the SHG scattering indicatrix at the maximum of the anisotropic dependence consists of two parts: a sharp peak in the specular direction and the background, which is SH radiation of lower intensity in a wide range of polar angles. At the minimum of the anisotropic dependence, the scattering indicatrix represents only the background, coinciding within the experimental error with the background attained for the maximum of the SHG scattering indicatrix. This means that the diffuse part of the signal is isotropic, while the specular part (minus the diffuse background) is completely anisotropic, i.e. it vanishes at the minima of the azimuthal dependence.

Aktsipetrov et al. [68] proposed a stochastic model of the microcrystalline structure of a film, in which the film is considered as a mixture of (111) and (100) crystallites with an arbitrary orientation of the polar axis in the film plane. The

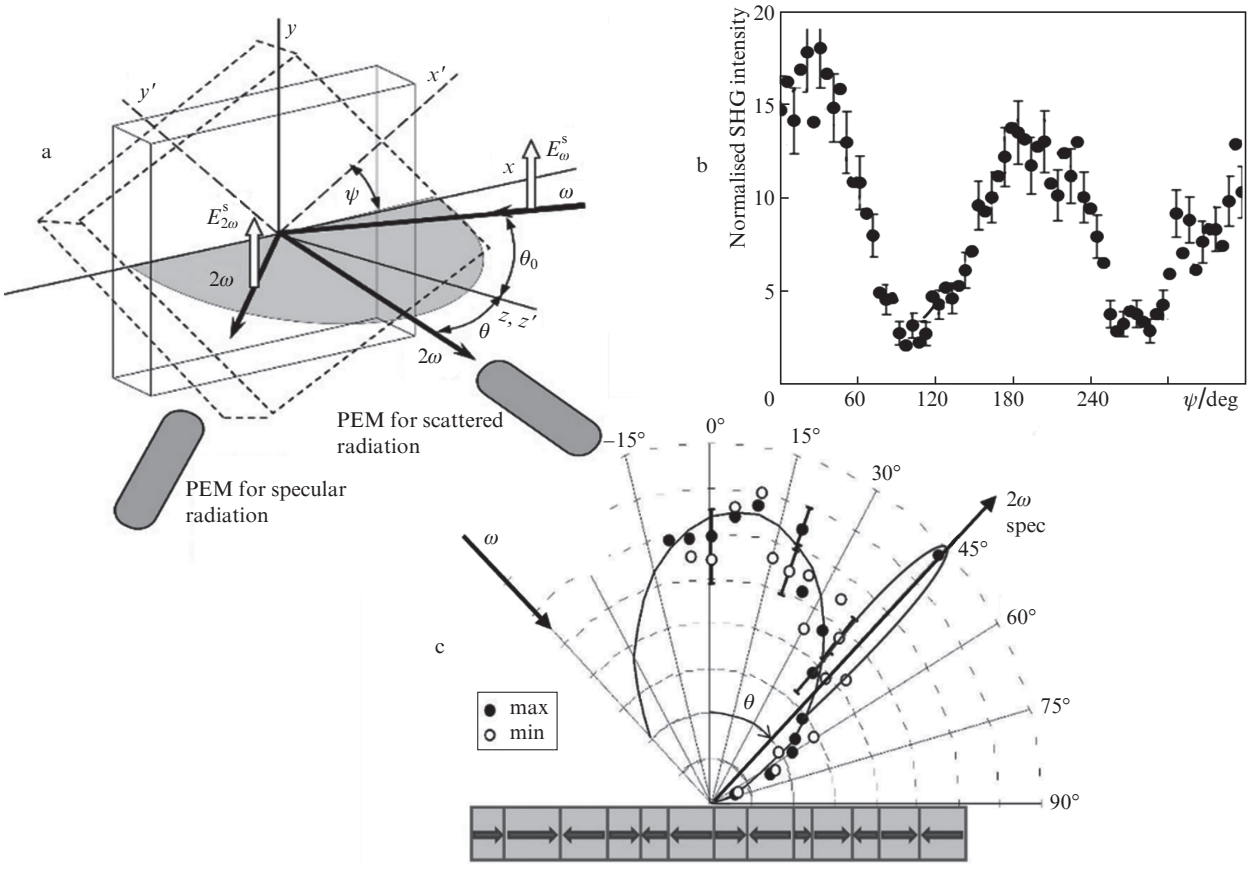

Figure 7. (a) Scheme of the geometry of the experiment to study the scattering indicatrix and the azimuthal dependence of the SHG intensity in textured PZT films. (b) Azimuthal dependence of $I_{2\omega}(\psi)$. (c) Scattering indicatrixes $I_{2\omega}(\theta)$ at the minimum and maximum of the azimuthal dependence; the line is the result of fitting within the framework of the model proposed in [72], and the maximum intensity of the scattered SHG is observed at $\theta = 10°$ and does not coincide with the mirror direction at $\theta = 45°$. The textured film is depicted as a set of microcrystallites of different sizes, whose different orientations in the film plane are schematically shown as arrows of different lengths.

shape of the SHG scattering indicatrix with a maximum shifted from the specular direction is determined by spatial fluctuations of the orientation of microcrystallites in the film plane, and the shift of the scattering maximum from the specular direction is caused by anticorrelations of microcrystallite orientation. Approximation of the shape of the SHG indicatrix yields a correlation length of about 250 nm, which corresponds to the average microcrystallite size in the film plane and indicates that anticorrelations arise mainly in neighbouring microcrystallites.

The SHG scattering technique (measurement of scattering diagrams or indicatrixes) for studying inhomogeneities in ferroelectrics was further developed in Refs [73–75].

6.2. Investigation of ferroelectric phase transitions by the SHG method

From the point of view of symmetry, ferroelectric phase transitions are transitions from a centrosymmetric paraphase to a noncentrosymmetric ferroelectric phase as the temperature decreases to T_C. These transitions are the simplest from the point of view of their study by the SHG method, since the transition to the noncentrosymmetric ferroelectric phase is accompanied by a sharp increase in the SHG intensity. Phase transitions in the bulk of crystals were observed almost immediately after the experimental discovery of SHG in crystals, since many widespread nonlinear optical crystals are ferroelectrics [76]. The studying ferroelectric phase transitions in thin films seems to be a more difficult task, especially if the ferroelectric is a complex multicomponent system, texture, or ceramic, and also has surface properties.

Papers [77, 78] present the results of studying two-dimensional organic polyvinylidene fluoride (PVDF) films obtained by the Langmuir–Blodgett (LB) technique. For the first time, the existence of ferroelectric ordering in two-dimensional systems (in films up to two monomolecular layers thick) was proved by the SHG method in LB films, and two phase transitions were discovered.

Figure 8 shows a schematic representation of an LB film with indication of all contributions to the nonlinear susceptibility and experimental temperature dependences of the SHG intensity in the vicinity of the surface phase transition for LB films with a thickness of 60 and 15 monolayers (Figs 8a and 8b, respectively). One can see that at a temperature below 30 °C, the dependence of the SHG intensity on temperature exhibits a pronounced peak at about 28 °C, and a further monotonic increase in the nonlinear response with the SHG signal reaching saturation occurs at a temperature below 10 °C. At temperatures above 35 °C, the SHG signal changes slightly, and as the temperature rises to about 100 °C, at which saturation occurs, the nonlinear response gradually increases. Sample cooling is accompanied by the appearance of a wide SHG intensity hysteresis loop with a maximum at approximately 80 °C. Similar dependences were observed for a film with a thickness of 15 monolayers.

These features of the SHG temperature dependences indicate the existence of two phase ferroelectric–paraelectric transitions. The first one is a phase transition with a film thickness-independent Curie temperature $T_C^B = 80$ °C, associated with the 3D ferroelectric state of the PVDF bulk material. The second phase transition of the first kind is observed at $T_C^S = 20$ °C; it corresponds to ferroelectric ordering in the

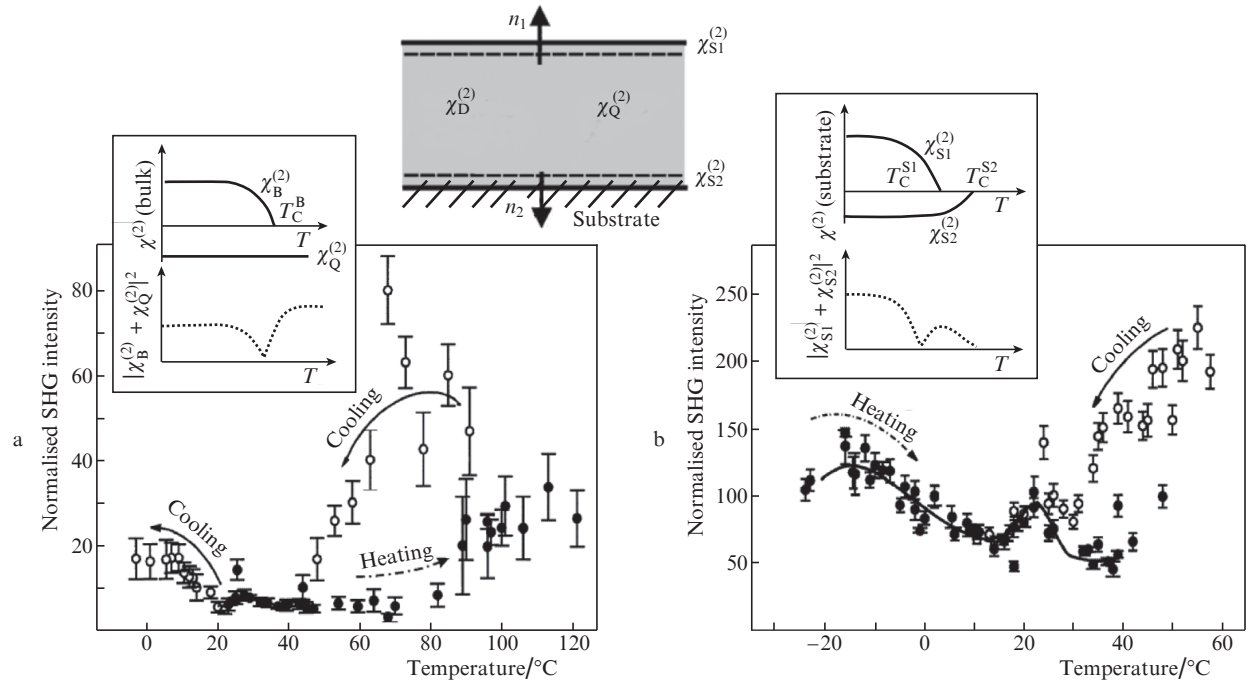

Figure 8. Experimental temperature dependences of the SHG intensity during cooling and heating of PVDF films (a) 60 and (b) 15 monolayers thick. The upper inset shows the diagram of a nonlinear optical model of a ferroelectric film, including the air–LB-film and LB-film–substrate interfaces with dipole quadratic susceptibilities (subscripts D and Q denote dipole and quadrupole susceptibilities, and subscripts S1 and S2 are surface susceptibilities, respectively). The other two insets show diagrams of the model temperature dependences of the surface and bulk susceptibilities and their interfering combination.

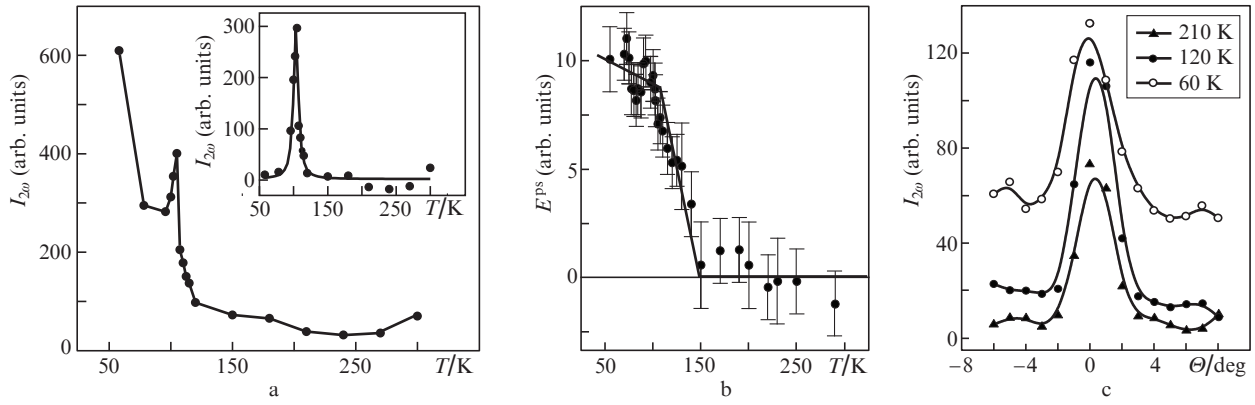

Figure 9. Temperature dependences of the SHG intensity scattered at a deviation from the specular reflection angle $\theta = 8°$ (a) and the field of the coherent SH in the specular direction (b); (c) SH scattering indicatrixes at different temperatures in a strontium titanate crystal; Θ is the scattering angle.

upper surface layer of the PVDF film. Modelling the dependences $I_{2\omega}(T)$ with allowance for the interference of various contributions (Fig. 8a, inset at the top) yields good agreement with the experimental results.

Papers [79, 80] present the results of detection and study of the structural phase transition in the near-surface region of the potential ferroelectric strontium titanate, $SrTiO_3(110)$, which has a bulk structural phase transition m3m → 4/mmm with a Curie temperature $T_C = 105$ K (Fig. 9).

The angular distribution of the SHG intensity shows the presence of two components: coherent radiation $I_{2\omega\,\mathrm{coh}}$ in the specular direction and incoherent radiation $I_{2\omega\,\mathrm{scat}}$ in a wide range of scattering angles: $I_{2\omega} = I_{2\omega\,\mathrm{scat}} + I_{2\omega\,\mathrm{coh}}$. The feature at $T = T_C$ is associated with critical opalescence during the structural phase transition of the bulk crystal. There is a temperature T^* at which the dependence undergoes a kink: at $T > T^*$ the intensity $I_{2\omega}$ is zero, and at $T_C < T < T^*$ it increases with decreasing temperature. At $T = T_C$, there is a kink in the temperature dependence of the SHG intensity. The dependences obtained for the field of the coherent SH are well described in terms of the Landau theory.

Thus, for single-crystal strontium titanate, based on the SHG study, the presence of a near-surface phase transition was established at a temperature $T^* = 150$ K, i.e., 45°C higher than the temperature of the bulk phase transition T_C. The temperature dependence of the order parameter is described by a power dependence with the exponent $\beta = 1/2$. The SHG intensity of the radiation scattered due to fluctuations of the volume order parameter is sufficiently high; against its background, critical scattering by the surface near the phase transition was not detected.

6.3. Polarisation switching

Since in most ferroelectrics there is nonswitchable polarisation (pinned domains) induced by the presence of electrodes (and near-electrode regions) and defects, which is especially important for thin films, then formula (1) can be rewritten in the form [81]:

$$I_{2\omega} \propto \left| \hat{\chi}_P^{(3)} \vdots (\boldsymbol{P}_0 + \boldsymbol{P}_E)\boldsymbol{E}_\omega \boldsymbol{E}_\omega \right|^2, \qquad (2)$$

where $\hat{\chi}_P^{(3)}$ is the third-order nonlinear susceptibility; $\boldsymbol{P}_E$ is the switchable (depending on the applied electric field) polarisation component; and $\boldsymbol{P}_0$ is the part of the ferroelectric polarisation that is not switched by the electric field and whose contribution to SHG is coherent to the contribution of the switched component. Expression (2) makes it possible to obtain the ratio of the switchable polarisation to the nonswitchable one, as well as the hysteresis loops of the dielectric polarisation.

This expression takes into account, and this is significant, that the main contribution to the SHG signal is made by domains with certain polarisation, i.e. the contribution is essentially crystallographic. This corresponds to the generally accepted statement of electro-optics, according to which the lattice makes the main contribution to the polarisability of a ferroelectric at optical frequencies [82]. At the same time, when saturation of the dielectric polarisation is reached, as in electro-optical effects, the dependence on the external field in the SHG signal is associated with the electronic polarisability, which manifests itself as a function of the field of optical constants, primarily the refractive index.

The ability of ferroics (ferroelectrics and magnets) to switch between two stable states is a basic principle of modern storage technology. However, with the absolute dominance of ferromagnetic materials in the market for memory devices, the possibilities of using ferroelectrics in such applications remain underestimated, despite the significant potential for their integration into semiconductor technologies [83].

One of the problems in the development of functional ferroelectric-based elements is the fundamental limitation imposed by the rate of polarisation switching. In particular, when an electric field is applied to a ferroelectric using electrodes and an electric field generator included in the electric circuit, the rate of polarisation switching between two stable states depends on the time characteristics of the employed devices. Optimisation of the electrode structure, as well as the development of alternative methods for generating pulses, including those using photoconductive switches, made it possible to achieve polarisation switching with a time constant of about 100 ps [84].

Advances in laser physics have led to the creation of high-power sources of electromagnetic pulses with a field amplitude of several tens of MV cm^{-1} and a duration of about 1 ps, which are used as a pump in the generation of radiation in the terahertz (THz) range. This contributed to the development of electrodeless methods for applying an electric field to a ferroelectric and, as a consequence, to the observation of new effects of THz excitation of coherent phonons of ultrafast dynamic switching.

To detect polarisation switching, the pump–probe method is used, in which pumping is performed by a THz pulse, and either optical or X-ray radiation is used as a probe. THz excitation of polarisation state switching processes, in turn, is based on two mechanisms: direct resonant excitation of a polar phonon by a broadband THz pulse with a frequency of 0.5–2.5 THz and a duration of 1 ps [85], or resonant excitation by a narrow-band and higher-frequency THz pulse of an IR active phonon associated with the polar phonon by the phonon–phonon interaction [86].

The theory of generation of coherent oscillations in pump–probe THz spectroscopy is described in [87]. The use of optical radiation as a probe makes it possible to distinguish between linear and nonlinear regimes of mode oscillations [88]; in this case, dynamic and, in the case of occurrence, permanent polarisation switching are recorded [89]. X-ray methods make it possible to directly measure the displacements of polar ions and the absolute value of the polarisation modulation (reversal) [85].

It is known that coherent phonons can be excited using optical pulses of femtosecond (50–100 fs) duration, while changes in the polarisation state of the ferroelectric caused by the action of a laser pulse, which can also be recorded in the experimental pump–probe scheme using optical or X-ray radiation as a probe, are similar to those described above for the case of THz pumping. Using this technique, polar phonons or soft modes in $LaAlO_3$ and $KMnF_3$ [90], as well as in ammonium sulfate [91], were studied, but the problem of searching for materials in which these effects would be most pronounced remains topical. In the pioneering work of a group led by A. Kimel [92, 93], it was suggested that the observation of an all-optical switching of the ferroelectric order parameter is most likely in a semiconductor ferroelectrics, where it is possible to lower the barrier for polar ions due to polarisation screening by photoexcited carriers in the conduction band.

6.4. Remote and ultrafast polarisation switching

The possibility of remote ultrafast control of the order parameter in ferroic materials (ferroelectrics, magnets, multiferroics) is promising for use in memory elements and for manipulation of light fluxes, primarily in an optical computer. To this end, it is necessary to switch the dielectric polarisation by an electromagnetic pulse. Moreover, for non-volatile memory elements, a long-term single switching is necessary, while for random access memory and modulators, dynamic (nonstationary) switching is sufficient. For remote switching, it is possible to use not only femtosecond optical pulses (of the visible and IR ranges), but also picosecond pulses of the THz range. Time dependences of polarisation under the action of an electromagnetic pulse are studied according to the optical (THz) pump/optical probe scheme.

How can switching of the dielectric (ion) polarisation be achieved by electromagnetic pulses? Under dynamic action, coherent phonons are excited by a short pulse. The idea is that if a polar (in particular, soft) mode with a significant amplitude is excited, then the transition of an ion is possible from one minimum of the potential well to another.

The ferroelectric polarisation $\boldsymbol{P}$ in an electric field, including an electromagnetic pulse, is described by the Landau–Khalatnikov equation

$$\frac{\mu^2}{\varepsilon_0}\frac{\mathrm{d}^2\boldsymbol{P}}{\mathrm{d}t^2}+\frac{\gamma\mu^2}{\varepsilon_0}\frac{\mathrm{d}\boldsymbol{P}}{\mathrm{d}t}=-\frac{\partial F}{\partial \boldsymbol{P}}+\boldsymbol{E}, \tag{3}$$

where μ is a coefficient containing the charge and mass numbers of the vibrational mode; γ is the attenuation coefficient; and $\boldsymbol{E}$ is the external electric field.

The two-minimum thermodynamic potential F for an ion is described in the simplest case by the expression

$$F=\frac{\alpha_2}{2}P^2+\frac{\alpha_4}{4}P^4, \tag{4}$$

where $\alpha_2 \propto T - T_C$ and α_4 are Landau expansion coefficients.

6.4.1. Optical pulse. The frequencies of optical radiation are much higher than phonon frequencies, and the excitation is nonresonant with respect to lattice vibrations. Therefore, the external field in equation (3) is assumed to be zero, and the optical momentum enters this equation in the form of initial conditions $P'(t=0)=0$, $P'(t=0)=P'_0$. In this case, coherent phonons (the initial push described by the initial condition) are excited during the electron–phonon interaction with electrons that were directly excited by the optical pulse.

Coherent phonons can be excited by optical pulses according to the pulsed stimulated Raman scattering scheme. In this case, the excitation is resonant, since for a pulse with a duration of 130 fs, the difference in frequencies corresponding to the edges of the pulse spectrum can be equal to the frequency of the soft mode. The experiments were carried out in KDP crystals [94], and the light intensity was measured at the diffraction maximum (in the case of diffraction by a phonon).

It should be noted that although there is soft mode excitation, switching is absent. One of the reasons is the presence of too much chaos (cells are not connected to each other, and everything is averaged).

6.4.2. Terahertz pulse. The THz range pulse is resonant to the soft mode. In equation (1), the external field can be represented in a form close to the experimentally observed one:

$$E_{\mathrm{THz}}(t)=A\exp(-4t^2/\tau^2)\operatorname{sinc}(2\pi t), \tag{5}$$

where A is the field amplitude, and τ is the pulse duration. The initial conditions are not of great importance in this case.

The solution to equation (4) with the right-hand side in the form of (5) allows one to obtain the dependence of the dielectric polarisation on time. We consider the initial state of the ferroelectric to be unpolarised: the number of ions in two possible minima (see insets in Fig. 10a) is the same. Substituting solution (3) into the expressions for $I_{2\omega}$, (1) or (2), we obtain the dependence $I_{2\omega}(t)$. An example of this dependence for a $BaSrTiO_3$ (BST) film is shown in Fig. 10. When a THz pulse is excited by a pulse of sufficient amplitude, the ion oscillates between two minima and can finally undergo a transition to the minimum that is opposite to the initial one, i.e. both dynamic and long-term polarisation switching occur. For a BST, excitation by a THz pulse is resonant, since the frequency of the soft mode at room temperature is 1.9 THz, i.e. it is rather close to the frequency maximum of the THz pulse (1.4 THz). It can be seen that the presented model (Fig. 10b) describes well the experimental dependences.

The results of the experiment and calculation are the dependences $I_{2\omega}(t)$ and $E_{\mathrm{THz}}(t)$. Thus, the SH hysteresis loop $I_{2\omega}(E_{\mathrm{THz}})$ is parametrically set (Fig. 10c). Using (2), one can

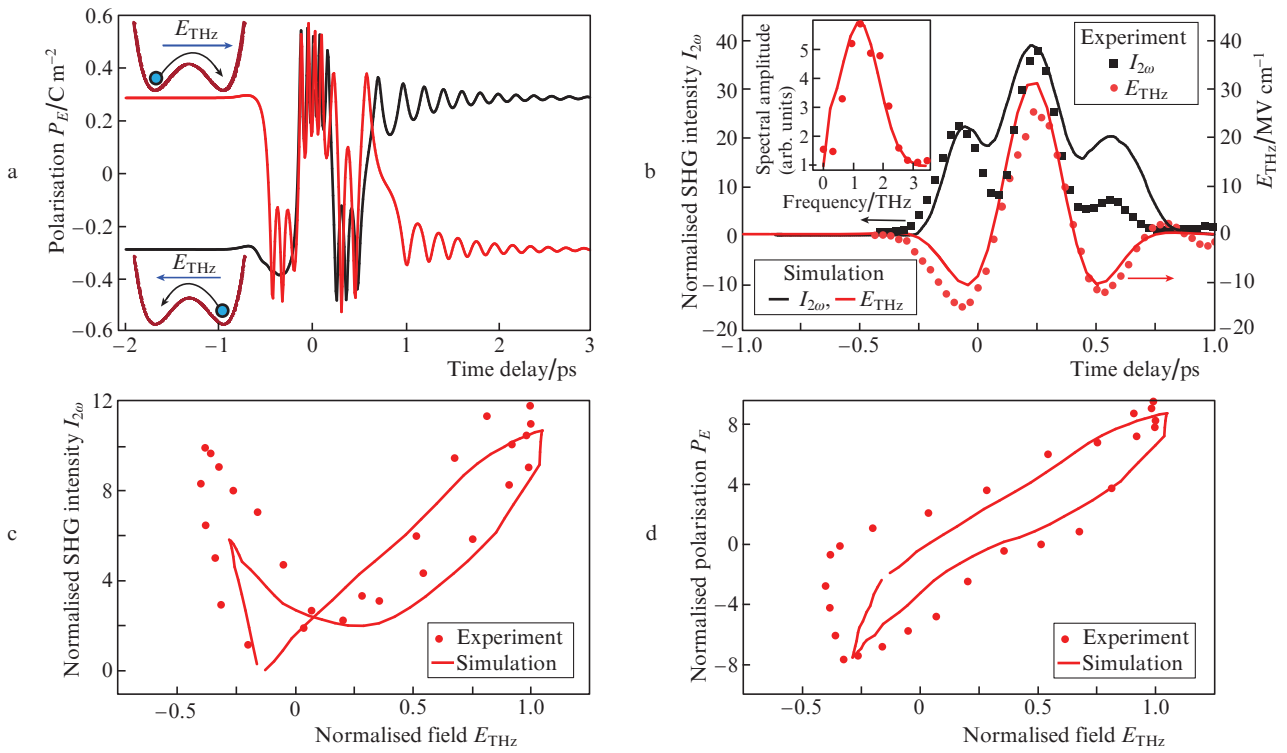

Figure 10. (Colour online) Calculated time dependences of (a) dielectric polarisation P_E and (b) SHG intensity and terahertz pulse field E_{THz}, as well as dependences of (c) SHG intensity and (d) polarisation P_E on the field E_{THz}. Insets show the position of the ion in the potential well; the maximum amplitude of the THz field is 30 MV cm^{-2}.

calculate the dielectric polarisation $\boldsymbol{P}_E$, i.e. obtain a conventional ferroelectric hysteresis loop (Fig. 10d). Note that in the calculation, we used the convolution of the optical and THz pulses when they were superimposed.

Thus, the resonant excitation of the soft mode leads to local polarisation switching. In this case, switching between initially opposite minima in the SHG signal is indistinguishable and, therefore, averaging over all elementary cells after the termination of the pulse leads to $I_{2\omega}(t \to \infty) \to 0$. Dynamic zeroing does not occur, since the minima are not equivalent with respect to the external field.

A well-known technique for separating a SHG signal whose sources have different signs is the use of interference with a source of a given nonlinear susceptibility [95–97]. This scheme was used in [86]. It was also shown there that the dielectric polarisation can be switched by resonant action on a higher-frequency polar mode. In this case, the excitation of the soft mode and the subsequent switching of the polarisation are achieved due to the phonon–phonon interaction.

7. Modern development of the SHG method

Without claiming to be a complete review of the modern use of the SHG method, we will present some recent examples of the development of those areas, the beginning of which was largely initiated by the works presented in this paper.

First of all, it should be noted that polarisation microscopy of SHG crystals, films and, most of all, biological fibres such as collagen has been developed. For biology, SHG microscopy has become, in fact, a standard method for determining the crystallographic structure of fibres, which has clear advantages over X-ray diffraction analysis. Methodical works [98–101] describe approaches that make it possible to determine the structure of a material not only qualitatively, but also quantitatively. Polarisation SHG microscopy is also routinely used to characterise new crystals, including organic ones [102], and the domain structure of ferroelectrics [103].

Polarisation SHG microscopy proved to be extremely effective for studying new van der Waals materials, especially mono- and bilayers. For such layers, the SHG method can easily determine the orientation of crystallites during their deposition on a substrate by both exfoliation and CVD methods [104–106], as well as the mechanical stresses arising during the deposition [107]. Of particular interest are interlayer excitons in molecular bilayers. For centrosymmetrically packed bilayers, the SHG efficiency sharply decreases. However, in the spectral region of excitation corresponding to interlayer exciton resonances, it is possible to achieve the SHG intensity from a bilayer that is comparable to the SHG intensity from a noncentrosymmetric monolayer. The application of an electric field leads to the removal of the degeneracy of interlayer excitons due to the Stark effect and to an increase in the SHG signal by two orders of magnitude [108]. A variety of physical effects have been found in van der Waals materials, which, combined with their two-dimensionality, make these materials unique; in many cases, the SHG method makes it possible to study these properties.

In photonic-crystal and plasmonic structures, SHG is used not only for diagnostics, but also for fabricating devices for nonlinear photonics. In connection with the best compatibility with the modern technological base, silicon nonlinear nanophotonics has received significant development. The removal of centrosymmetry and enhancement of SHG in such structures is achieved due to electrically induced effects at the interfaces and resonances in nanoplasmonic structures deposited on the silicon surface [109]. Other materials that are

placed inside nanoresonators or bonded to metasurfaces are also used to enhance SHG [110–114]. The magnetic properties of two-dimensional structures and hidden boundaries, as well as the features of the magnetic nonlinear optical response and local field effects in plasmonic magnetic nanostructures and crystals, are also currently being studied using the SHG method [115–118].

8. Conclusions

This paper provides an overview of some of the works performed at the Chair of Quantum Electronics, Lomonosov Moscow State University, demonstrating unique possibilities of the SHG method for studying a wide class of structures based on centrosymmetric media, as well as ferroelectric ones. Our goal was not to describe all the studies carried out by our team in the field of SHG, especially in obtaining highly efficient conversion in nonlinear crystals. On the contrary, we tried to present less standard experiments, in which the analysis of parameters of the nonlinear response of various systems that included intensity, polarisation, and phase of the SH radiation, as well as the symmetry of nonlinear polarisation at the SH frequency, made it possible to reveal a number of parameters of the studied systems that did not appear in linear response. This applies, first of all, to separating the contribution of the surface nonlinearity of a number of resonant nanostructures and photonic crystals against the background of the 'bulk' quadrupole in the case of the Si/SiO_2 interface.

The reviewed papers present the foundations of the methodology for studying nano- and microstructures using a group of approaches based on SHG and its modification by external influences. They were carried out within the framework of international cooperation with representatives of advanced research centres – the University of Texas (Austin, USA), the Catholic University (Leuven, Belgium), the Radbout University in Nijmegen (Netherlands), the Laser Center (Göttingen, Germany) and others, which also reflects significant interest of scientists all over the world to the considered problems of nonlinear optical effects. At present, similar studies are being developed on the basis of a more modern experimental and technological base. Almost all of them are performed using femtosecond laser sources, and the temporal dynamics of nonlinear optical processes and the response of a substance to an intense laser impact at ultrashort times are analysed. However, the unique sensitivity of the optical SHG to the properties of surfaces, interfaces, and nanostructures is still used, which determines the relevance of considering the earlier works presented in this review.

Acknowledgements. The authors are grateful to their teacher and colleague Oleg Andreevich Aktsipetrov, founder of the Laboratory of Nonlinear Optics of Nanostructures and Photonic Crystals, Department of Quantum Electronics, Faculty of Physics, Lomonosov Moscow State University.

This work was supported by the Russian Foundation for Basic Research (Grant Nos 20-52-7819, 19-02-00826, and 18-02-40027).

References

1. Franken P.A., Hill A.E., Peters C.W., Weinreich G. *Phys. Rev. Lett*., **7**, 118 (1961).
2. Bloembergen N., Chang R.K., Lee C.H. *Phys. Rev*., **16** (22), 986 (1966).
3. Aktsipetrov O.A., Fedyanin A.A., Golovkina V.N., Murzina T.V. *Opt. Lett*., **19** (18), 1450 (1994).
4. Cheng R.K., Furtak T. (Eds) *Surface-Enhanced Raman Scattering* (New York: Plenum Press, 1981; Moscow: Mir, 1984).
5. Koroteev N.I., Shumai I.L. *Fizika moshchnogo lazernogo izlucheniya* (Physics of High-Power Laser Radiation) (Moscow: Nauka, 1991).
6. Shen Y.R. P*rinciples of Nonlinear Optics* (New York: Wiley, 1984; Moscow: Nauka, 1989).
7. Boyd R. *Nonlinear Optics* (London: Academic Press, 1992).
8. Akhmediev N.N., Borisov S.B., Zvezdin A.K., Lyubchanskii I.L., Melikhov Yu.V. *Fiz. Tverd. Tela*, **27**, 1075 (1985).
9. Aktsipetrov O.A., Braginskii O.V., Esikov D.A. *Sov. J. Quantum Electron*., **20**, 259 (1990) [*Kvantovaya Elektron*., **17**, 320 (1990)].
10. Pan R.P., Wei H.D., Shen Y.R. *Phys. Rev. B*, **39**, 1229 (1989).
11. Reif J., Zink J.C., Schneider C.-M., Kirschner J. *Phys. Rev. Lett*., **67**, 2878 (1991).
12. Aktsipetrov O.A. *Colloids and Surfaces A*, **202**, 165 (2002).
13. Aktsipetrov O.A., Baranova I.M., Evtyukhov K.N. *Second Order Nonlinear Optics of Silicon and Silicon Nanostructures* (London: CRC Press, Taylor & Francis Group., 2016).
14. Tom H.W.K., Heinz T.F., Shen Y.R. *Phys. Rev. Lett*., **51** (21), 1983 (1983).
15. Aktsipetrov O.A., Baranova I.M., Il'inskii Yu.A. *Sov. Phys. JETP*, **64**, 167 (1986) [*Zh. Eksp. Teor. Fiz*., **91** (1), 287 (1986)].
16. Sipe J.E., Moss D.J., van Driel H.M. *Phys. Rev. B*, **35** (3), 1129 (1987).
17. Aktsipetrov O.A., Baranova I.M., Esikov D.A., Kulyuk D.A., Mishina E.D., Strumban E.E., Tsytsanu V.I., Raceev S.A. *Dokl. Akad. Nauk SSSR*, **294** (3), 579 (1987).
18. Baranova I.M., Evtyukhov K.N. *Quantum Electron*., **27** (4), 336 (1997) [*Kvantovaya Elektron*., **24** (4), 347 (1997)].
19. Schuhmacher D., Marowsky G., Fedyanin A.A., Dolgova T.V., Aktsipetrov O.A. *Mat. Sci. Sem. Process.*, **4**, 51 (2001).
20. Kulyuk L.L., Shutov D.A., Strumban E.E., Aktsipetrov O.A. *J. Opt. Soc. Am. B*, **8** (8), 1766 (1991).
21. Aktsipetrov O.A., Fedyanin A.A., Melnikov A.V., Mishina E.D., Rubtsov A.N., Anderson M.H., Wilson P.T., ter Beek M., Hu X.F., Dadap J.I., Downer M.C. *Phys. Rev. B*, **60** (12), 8924 (1999).
22. Van Hasselt C.W., Devillers M.A.C., Rasing Th., Aktsipetrov O.A. *J. Opt. Soc. Am. B*, **12** (1), 33 (1995).
23. Aktsipetrov O.A., Fedyanin A.A., Mishina E.D., Nikulin A.A., Rubtsov A.N., van Hasselt C.W., Devillers M.A.C., Rasing Th. *Phys. Rev. Lett*., **78** (1), 46 (1997).
24. Aktsipetrov O.A., Mishina E.D., Nikulin A.A., Rubtsov A.N., Fedyanin A.A., van Hasselt C.W., Devillers M.A.C., Rising Th. *Dokl. Ross. Akad. Nauk*, **348**, 37 (1996).
25. Heinz T.F., Himpsel F.J., Palange E., Burstein E. *Phys. Rev. Lett*., **63** (6), 644 (1989).
26. Dadap J.I., Xu Z., Hu X.F., Downer M.C., Russell N.M., Ekerdt J.G., Aktsipetrov O.A. *Phys. Rev. B*, **56** (20), 13367 (1997).
27. Aktsipetrov O.A., Dolgova T.V., Fedyanin A.A., Schuhmacher D., Marowsky G. *Thin Sol. Films*, **364**, 91 (2000).
28. Dolgova T.V., Fedyanin A.A., Aktsipetrov O.A., Marowsky G. *Phys. Rev. B*, **66** (3), 033305 (1-4) (2002).
29. Dolgova T.V., Schuhmacher D., Marowsky G., Fedyanin A.A., Aktsipetrov O.A. *Appl. Phys. B*, **74**, 653 (2002).
30. Lee C.H., Chang R.K., Bloembergen N. *Phys. Rev. Lett*., **18** (5), 167 (1967).
31. Aktsipetrov O.A., Mishina E.D. *Dokl. Akad. Nauk SSSR*, **274** (1), 62 (1984).
32. Aktsipetrov O.A., Baranova I.M., Grigor'eva L.V., Evtyukhov K.N., Mishina E.D., Murzina T.V., Chernyi I.V. *Sov. J. Quantum Electron*., **21**, 854 (1991) [*Kvantovaya Elektron*., **18** (8), 943 (1991)].
33. Aktsipetrov O.A., Baranova I.M., Evtyukhov K.N., Murzina T.V., Chernyi I.V. *Sov. J. Quantum Electron*., **22**, 807 (1992) [*Kvantovaya Elektron*., **19** (9), 869 (1992)].
34. Aktsipetrov O.A., Fedyanin A.A., Mishina E.D., Rubtsov A.N., van Hasselt C.W., Devillers M.A.C. *Rasing Th. Phys. Rev. B*, **54** (3), 1825 (1996).
35. Aktsipetrov O.A., Fedyanin A.A., Mishina E.D., Rubtsov A.N., van Hasselt C.W., Devillers M.A.C., Rasing Th. *Surf. Sci*., **352–354**, 1033 (1996).

36. Baranova I.M., Evtyukhov K.N. *Quantum Electron*., **25** (12), 1198 (1995) [*Kvantovaya Elektron*., **22** (12), 1235 (1995)].
37. Dadap J.I., Hu X.F., Anderson M.H., Downer M.C., Lowell J.K., Aktsipetrov O.A. *Phys. Rev. B*, **53** (12), R7607 (1996).
38. Dolgova T.V., Fedyanin A.A., Aktsipetrov O.A. *Phys. Rev. B*, **68** (7), 073307 (2003).
39. Aktsipetrov O.A., Fedyanin A.A., Melnikov A.V., Dadap J.I., Hu X.F., Anderson M.H., Downer M.C., Lowell J.K. *Thin Sol. Films*, **294**, 231 (1997).
40. Mishina E.D., Tanimura N., Nakabayashi S., Aktsipetrov O.A., Downer M.C. *Jpn. J. Appl. Phys*., **42**, 6731 (2003).
41. Dolgova T.V., Avramenko V.G., Nikulin A.A., Marowsky G., Pudonin A.F., Fedyanin A.A., Aktsipetrov O.A. *Appl. Phys. B*, **74**, 671 (2002).
42. Berreman D.W. *Phys. Rev*., **163**, 855 (1967).
43. Aktsipetrov O.A., Dubinina E.M., Elovikov S.S., Mishina E.D., Nikulin A.A., Novikova N.N., Strebkov M.S. *JETP Lett*., **44** (8), 371 (1988) [*Pis'ma Zh. Eksp. Teor. Fiz*., **48**, 92 (1988)].
44. Kim E.M., Elovikov S.S., Murzina T.V., Nikulin A.A., Aktsipetrov O.A. *Phys. Rev. Lett*., **95**, 227402 (2005).
45. Didenko N.V., Kim E.M., Muzychenko D.A., Nikulin A.A., Aktsipetrov O.A. *Appl. Phys. B*, **74**, 647 (2002).
46. Kolmychek I.A., Mamonov E.A., Bochenkov V.E., Murzina T.V. *Opt. Lett*., **34** (22), 5473 (2019).
47. Bochenkov V.E., Sutherland D.S. *Nano Lett*., **13**, 1216 (2013).
48. Krutyanskiy V.L., Kolmychek I.A., Gan'shina E.A., Murzina T.V., Evans P., Pollard R., Stashkevich A.A., Zayats A. *Phys. Rev. B*, **87**, 035116 (2013).
49. Kruk S., Weismann M., Bykov A.Y., Mamonov E.A., Kolmychek I.A., Murzina T.V., Panoiu N.C., Neshev D.N., Kivshar Y.S. *ACS Photonics*, **2** (8), 1007 (2015).
50. Kolmychek I.A., Bykov A.Y., Mamonov E.A., Murzina T.V. *Opt. Lett*., **40** (16), 3758 (2015).
51. Kolmychek I.A., Shaimanov A.N., Baryshev A.V., Murzina T.V. *Opt. Lett*., **41** (23), 5446 (2016).
52. Albooyeh M., Kruk S., Menzel C., Helgert C., Kroll M., Krysinski A., Decker M., Neshev D.N., et al. *Sci. Rep*., **4**, 4484 (2014).
53. Armelles G., Cebollada A., Garcia-Martin A., Gonzalez M.U. *Adv. Opt. Mater*., **1**, 10 (2013).
54. Yablonovitch E. *Phys. Rev. Lett*., **58**, 2059 (1987).
55. Dolgova T.V., Maidykovski A.I., Martemyanov M.G., Marowsky G., Mattei G., Schumacher D., Yakovlev V.A., Fedyanin A.A., Aktsipetrov O.A. *JETP Lett*., **73** (1), 6 (2001) [*Pis'ma Zh. Eksp. Teor. Fiz*., **73** (1), 8 (2001)].
56. Gusev D.G., Soboleva I.V., Martemyanov M.G., Dolgova T.V., Fedyanin A.A., Aktsipetrov O.A. *Phys. Rev. B*, **68**, 233303 (2003).
57. Dolgova T.V., Maidykovski A.I., Martemyanov M.G., Fedyanin A.A., Aktsipetrov O.A. *J. Opt. Soc. Am. B*, **19** (9), 2129 (2002).
58. Dolgova T.V., Maidykovski A.I., Martemyanov M.G., Fedyanin A.A., Aktsipetrov O.A., Marowsky G., Yakovlev V.A., Mattei G. *Appl. Phys. Lett*., **81** (15), 2725 (2002).
59. Soboleva I.V., Murchikova E.M., Fedyanin A.A., Aktsipetrov O.A. *Appl. Phys. Lett*., **87**, 241110 (2005).
60. Murzina T.V., Kolmychek I.A., Maidykovski A.I., Nikulin A.A., Sychev F.Yu., Aktsipetrov O.A. *Opt. Lett*., **33** (22), 2581 (2008).
61. Martemyanov M.G., Kim E.M., Dolgova T.V., Fedyanin A.A., Aktsipetrov O.A., Marowsky G. *Phys. Rev. B*, **70**, 073311 (2004).
62. Soboleva I.V., Seregin S.A., Fedyanin A.A., Aktsipetrov O.A. *J. Opt. Soc. Am. B*, **28**, 1680 (2011).
63. Murzina T.V., Kim E.M., Kapra R.V., Moshnina I.A., Aktsipetrov O.A., Kurdyukov D.A., Kaplan S.F., Golubev V.G., Bader M.A., Marowsky G. *Appl. Phys. Lett*., **88** (2), 022501 (2006).
64. Dolino G., Lajzerowicz J., Vallade M. *Phys. Rev. B*, **2**, 2194 (1970).
65. Miller R.C., Kleinman D.A., Savage A. *Phys. Rev. Lett*., **11**, 146 (1963).
66. Savage A., Miller R.C. *Appl. Opt*., **1**, 661 (1962).
67. Weinmann D., Vogt H. *Phys. Stat. Sol*., **23**, 463 (1974).
68. Aktsipetrov O.A., Apukhtina S.B., Vorotilov K.A., Mishina E.D., Nikulin A.A., Sigov A.S. *JETP Lett*., **54**, 582 (1991) [*Pis'ma Zh. Eksp. Teor. Fiz.*, **54**, 562 (1991)].
69. Aktsipetrov O.A., Vorotilov K.A., Klimkin D.A., Mishina E.D., Nikulin A.A., Sigov A.S., Fedyanin A.A., Devilers M.A.C., Rasing Th. *Fiz. Tverd. Tela*, **38**, 3101 (1996).
70. Aktsipetrov O.A., Fedyanin A.A., Klimkin D.A., Nikulin A.A., Mishina E.D., Sigov A.S., Vorotilov K.A., Van Hasselt C.W., Devillers M.A.C., Rasing T. *Ferroelectrics*, **186**, 215 (1996).
71. Aktsipetrov O.A., Fedyanin A.A., Klimkin D.A., Nikulin A.A., Mishina E.D., Sigov A.S., Vorotilov K.A., Devillers M.A.C., Rasing T. *Ferroelectrics*, **190**, 143 (1997).
72. Melnikov A.V., Nikulin A.A., Aktsipetrov O.A. *Phys. Rev. B*, **67**, 134104 (2003).
73. Shan J.-Y., de la Torre A., Laurita N.J., Zhao L., Dashwood C.D., Puggioni D., Wang C.X., Yamaura K., Shi Y., Rondinelli J.M., Hsieh D. *Phys. Rev. Res*., **2**, 033174 (2020).
74. Wang B., Cojocaru C., Krolikowski W., Switkowski K., Sheng Y., Akhouayri H., Vilaseca R., Scalora M., Trull J. *19th International Conference on Transparent Optical Networks (ICTON)* (IEEE, 2017) pp 1–3.
75. Zhang Y., Zhang Y., Guo Q., Zhong X., Chu Y., Lu H., Zhong G., Jiang J., Tan C., Liao M., Lu Z., Zhang D., Wang J., Yuan J., Zhou Y. *Comput. Mater*., **4**, 39 (2018).
76. Miller R.C. *Phys. Rev*., **134**, A1313 (1964).
77. Aktsipetrov O.A., Misuryaev T.V., Murzina T.V., Blinov L.M., Fridkin V.M., Palto S.P. *Opt. Lett*., **25**, 411 (2000).
78. Aktsipetrov O.A., Blinov L.M., Fridkin V.M., Misuryaev T.V., Murzina T.V., Palto S.P., Yudin S.G. *Surf. Sci*., **454–456**, 1016 (2000).
79. Mishina E.D., Misuryaev T.V., Sherstyuk N.E., Lemanov V.V., Morozov A.I., Sigov A.S., Rasing T. *Phys. Rev. Lett*., **85**, 3664 (2000).
80. Mishina E.D., Morozov A.I., Sigov A.S., Sherstyuk N.E., Aktsipetrov O.A., Lemanov V.V., Rasing Th. *J. Exp. Theor. Phys*., **94** (3), 552 (2002) [*Zh. Eksp. Teor. Fiz*., **121**, 644 (2002)].
81. Mishina E.D., Sherstyuk N.E., Pevtsov E.P., Vorotilov K.A., Sigov A.S., Moret M.P., Rössinger S.A., Larsen P.K., Rasing T. *Appl. Phys. Lett*., **78**, 796 (2001).
82. Waser R., Bottger U., Tiedke S. (Eds) *Polar Oxides* (New York: Wiley, 2004).
83. Scott J.F. *Ferroelectrics*, **503**, 117 (2016).
84. Li J., Nagaraj B., Liang H., Cao W., Lee C.H., Ramesh R. *Appl. Phys. Lett*., **84**, 1174 (2004).
85. Kozina M., van Driel T., Chollet M., Sato T., Glownia J.M., Wandel S., Radovic M., Staub U., Hoffmann M.C. *Struct. Dyn*., **4**, 054301 (2017).
86. Mankowsky R., von Hoegen A., Först M., Cavalleri A. *Phys. Rev. Lett*., **118**, 197601 (2017).
87. Udina M., Cea T., Benfatto L. *Phys. Rev. B*, **100**, 165131 (2019).
88. Kozina M., Fechner M., Marsik P., van Driel T., Glownia J.M., Bernhard C., Radovic M., Zhu D., Bonetti S., Staub U., Hoffmann M.C. *Nat. Phys*., **15**, 387 (2019).
89. Salén P., Basini M., Bonetti S., Hebling J., Krasilnikov M., Nikitin A.Y., Shamuilov G., Tibai Z., Zhaunerchyk V., Goryashko V. *Phys. Rep*., **836–837**, 1 (2019).
90. Kohmoto T., Masui M., Abe M., Moriyasu T., Tanaka K. *Phys. Rev. B*, **83**, 064304 (2011).
91. Hauf C., Hernandez Salvador A.-A., Holtz M., Woerner M., Elsaesser T. *Struct. Dyn*., **5**, 024501 (2018).
92. Brekhov K.A., Grishunin K.A., Afanas'ev D.V., Semin S.V., Sherstyuk N.E., Kitaeva G.Kh., Mishina E.D., Rasing Th., Kimel A.V. *JETP Lett*., **102**, 372 (2015) [*Pis'ma Zh. Eksp. Teor. Fiz*., **102** (6), 410 (2015)].
93. Kimel A.V., Kalashnikova A.M., Pogrebna A., Zvezdin A.K. *Phys. Rep*., **852**, 1 (2020).
94. Yoshioka S., Tsujimi Y., Yagi T. *J. Phys. Soc. Jpn*, **67**, 377 (1998).
95. Kurimura S., Uesu Y. *J. Appl. Phys*., **81**, 369 (1997).
96. Aktsipetrov O.A., Mishina E.D., Misuryaev T.V., Nikulin A.A., Novak V., Stolle R., Rasing T. *Surf. Sci*., **402–404**, 576 (1998).
97. Aktsipetrov O.A., Fedyanin A.A., Nikulin A.A., Mishina E.D., Sigov A.S., Sherstyuk N.E. *Ferroelectrics*, **218**, 1 (1998).
98. Cisek R., Joseph A., Harvey M., Tokarz D. *Front. Phys*., **9**, 726996 (2021).
99. Mostaço-Guidolin L., Rosin N.L., Hackett T.L. *Int. J. Mol. Sci*., **18**, 1772 (2017).
100. Hristu R., Stanciu S.G., Tranca D.E., Stanciu G.A. *J. Biophotonics*, **10**, 1171 (2017).
101. Goto A., Otomo K., Nemoto T. *Front. Phys*., **7**, 56 (2019).
102. Pradeep V.V., Mitetelo N., Annadhasan M., Popov M., Mamonov E., Murzina T., Chandrasekar R. *Adv. Opt. Mater*., **8**, 1901317 (2020).

103. Zhang Y., Zhang Y., Guo Q., Zhong X., Chu X., Lu H., Zhong G., Jiang J., Tan C., Liao M., Lu Z., Zhang D., Wang J., Yuan J., Zho Y. *Npj Comput. Mater.*, **4**, 39 (2018).
104. Mishina E., Sherstyuk N.E., Lavrov S.D., Sigov A.S. *Appl. Phys. Lett*., **106** (13), 131901 (2015).
105. Wang Y., Xiao J., Yang S., Wang Y., Zhang X. *Opt. Mater. Express*, **9**, 1136 (2019).
106. Liu J., Lo Tsz W., Sun J., Yip C.T., Lam C.T., Lei D.Y. *J. Mater. Chem. C*, **5**, 11239 (2017).
107. Mennel L., Paur M., Muelle T. *APL Photonics*, **4**, 034404 (2019).
108. Shree S., Lagarde D., Lombez L., Robert C., Balocchi A., Watanabe K., Taniguchi T., Marie X., Gerber I.C., Glazov M.M., Golub L.E., Urbaszek B., Paradisanos I. *Nat. Commun*., **12**, 6894 (2021).
109. Bhowmik G., An Y.Q., Schujman S., Diebold A.C., Huang M. *J. Appl. Phys*., **128**, 165106 (2020).
110. Li G.-C., Lei D., Qiu M., Jin W., Lan S., Zayats A.V. *Nat. Commun*., **12**, 4326 (2021).
111. Jin J., Lu J., Zhen B. *Nanophotonics*, **10** (17), 4233 (2021).
112. Fedotova A., Younesi M., Sautter J., Vaskin A., Löchner F.J.F., Steinert M., Geiss R., Pertsch Th., Staude I., Setzpfandt F. *Nano Lett*., **20** (12), 8608 (2020).
113. Huang Z., Wang M., Li Y., Shang J., Li K., Qiu W., Dong J., Guan H., Chen Z., Lu H. *Nanotechnology*, **21**, 32 (2021).
114. Ding Y., Wei C., Su H., Sun S., Tang Z., Wang Z., Li G., Liu D., Gwo S., Dai J., Shi J. *Adv. Opt. Mater*., **9** (16), 2100625 (2021).
115. Ma H., Liang J., Hong H., Liu K., Zou D., Wu M., Liu K. *Nanoscale*, **12**, 22891 (2020).
116. Ullah K., Meng Y., Shi Y., Wang F. *Adv. Opt. Mater*. (2022) (in press).
117. Ding S.-J., Zhang H., Yang D.-J., Qiu Y.-H., Nan F., Yang Z.-J., Wang J., Wang Q.-Q., Lin H.-Q. *Nano Lett.*, **19**, 2005 (2019).
118. Yang D., Im S., Pan G., Ding S., Yang Z., Hao Z., Zhou L., Wang Q. *Nanoscale*, **9**, 6068 (2017).